ICE-CAMERA: a flatbed scanner to study inland Antarctic polar precipitation.

Massimo del guasta

Istituto Nazionale Ottica CNR, Sesto Fiorentino, 50019, Firenze, Italy

Correspondence to: Massimo Del Guasta (massimo.delguasta@ino.cnr.it)

Abstract.

Studying precipitation at very high latitudes is difficult because of the harsh environmental conditions that limit the external activity of humans and instruments, especially in the polar winter. The direct monitoring of ice crystal habits and size distribution in antarctic precipitation is important for the validation of the algorithms used for retrieving precipitation from ground-based and satellite-borne radar instruments, and for the improvement of the climatological modeling of polar areas. The paper describes an automated device (ICE-CAMERA) specifically developed for the imaging, measurement and classification of ice precipitation on the Antarctic high plateau. The instrument gives detailed information on precipitation on an hourly basis. The article provides a description of the device and its image processing software. Starting in 2014, the instrument operates *almost* unattended all year round at Concordia station, Antarctica (75°S, 123°E, 3220 m altitude).

1. Introduction.

In Antarctica, the characteristics of ice precipitation depend greatly on the region. In coastal areas, precipitation is influenced by synoptic scale features, such as cyclones and fronts (Bromwich, 1988). In the interior (> 2500 m), a significant part of the precipitation falls in the form of small ice crystals ("diamond dust", DD) under clear-sky conditions (Fujita and Abe, 2006). Snow particles over Antarctica are generally smaller compared to other regions of the world. The largest particles are found close to the coast, where more water vapour is available and diameters up to 10 mm are recorded (Konishi et al., 1992) with particle shapes similar to mid-latitude ones (Satow, 1983). Most of the bigger particles are aggregates (some can be found in the dataset of Grazioli et al.,2022). More inland stations record snowflakes of much smaller sizes, ranging from particles smaller than 100 μm at South Pole (Walden et al., 2003, Lawson et al., 2006) till hundreds of μm at other inland stations (Lachlan-Cope et al., 2001).

In situ measurements of precipitation are rare in Antarctica and affected by large uncertainties. This is particularly true in the high plateau, where less than 20 cm of snow accumulates every year (Palerme et al.,2014). As a result, the global precipitation products that rely on these observations (i.e. the Global Precipitation Climatology Centre (GPCC), (Schneider et al., 2017)) have no coverage over this region. Other observational products, such as the Global Precipitation Climatology Project (GPCP) (Huffman et al.,2001) , that uses GPCC for bias correction over land, has relied on satellite-only precipitation estimates. Satellite products also face large uncertainties over cold regions such as Antarctica due to insufficient sensitivity of sensors to detect and estimate precipitation signals, complex surface emissivities, and poor understanding of precipitation microphysics. Ground based K-band radars (~1-cm wavelength) are robust instruments successfully employed for studying precipitation in coastal Antarctic sites (Souverijns et al., 2017) but are quite blind to the sub-millimetre ice particles encountered on the plateau, due to the relationship D^6 between the radar scattering cross-section and the particle diameter (D).

 The satellite-borne radar CloudSat (Liu, 2008) did provide a quantum leap in observing ice in the Antarctic atmosphere (up to 82 °S), but being a single-frequency radar (like K-band radars), the retrieval of precipitation quantities relies on many assumptions about the properties of particles, resulting into ±50% uncertainties for IWC (Heymsfield et al.,2008). The microphysical assumptions (shapes and size distribution of particles) are the biggest causes for IWC, IWP, and snowfall rate retrieval uncertainty (Hiley et al.,2011, Wood et al.,2015). Moreover, CloudSat bins close to the ground cannot be used for precipitation retrieval, resulting into a severe underestimation of the diamond-dust and blowing-snow contribution to Antarctic snow balance (Palm et al., 2018). Despite these uncertainties, in absence of ground validation CloudSat data are now used as

independent dataset for the validation of precipitation models in Antarctica (Palerme et al.,2014, Palerme et al.,2017). The direct observation and the continuous monitoring of habit and size distribution of precipitation is therefore required in order to validate both precipitation models, CloudSat and radar algorithms on the Antarctic plateau.

Disdrometers are robust *in-situ* devices, increasingly used in Antarctic coastal areas (Souverijns et al., 2017, Bracci et al.,2022). They provide the size distribution and falling speed of hydrometers, but they give no direct information about the shape. The evolution of disdrometers into 2D-disdrometers gave access to some shape indications about hydrometeors (Grazioli et al.,2014). A further evolution of disdrometers into Imaging-disdrometers, such as the Snowflake Video Imager (SVI) (Newman et al., 2009), provided realistic images of the crystals. Grazioli et al., (2017), as part of a multidisciplinary field campaigns, deployed a multi-angle snowflake camera (MASC) to take photographs of individual snow particles. This instrument, representing a further advance in the field of imaging disdrometers, collects high-resolution stereoscopic photographs of snowflakes in free fall while they cross the sampling area (Garrett et al., 2012), thus providing information about snowfall microphysics (Praz et al., 2017). The optical structure of the imaging-disdrometer and the MASC makes these instruments reliable in the presence of millimetre-sized hydrometeor precipitation. In Antarctica, their practical application is mostly limited to coastal zones where particles are coarse (e.g. MASC resolution is 33 μm).

The direct observation of inner Antarctic particles requires imaging techniques with resolution of a few microns. Photographic studies of precipitation in the interior of the Antarctic are quite rare, carried out primarily at the South Pole Station (SPS) through formvar replicas. In early works with formvar, Hogan (1975) identified at SPS millimetre-sized columnar crystals and column- and bullet-rosettes in cloud precipitation, and smaller ($\cong$100 μm diameter) platelike particles in clear-sky precipitation. Satow (1983), working with formvar replicas on Mizuho plateau found prevalently single bullets and combination of bullets. Long solid column crystals were also found (with an air temperature range from -42°C to -56°C) with a mean length of 290 μm and a maximum length of 1.2 mm, with a mean aspect ratio of 18. Small (50-400 μm) hexagonal, triangular, scalene and square plates were also observed. Kikuchi and Hogan (1979) collected formvar replicas of DD in the summer at SPS, finding columnar crystals of 90 μm average lengths and plates as small as 50 μm in diameter. Ohtake and Yogi (1979) classified winter ice crystal precipitation in Antarctica under six categories. These included large rosettes, bullets and columns (millimetre-sized), thin hexagonal plates and columns (200 μm or less), and smaller crystals of various shapes including triangular and polyhedral. Shimizu (1963) observed "long column" crystals in the winter at Byrd Station (80S, 120W). Size distributions of Antarctic DD in winter and spring were reported by Smiley et al. (1980) for particles larger than 50 um: they observed the same ice crystal forms that were reported earlier. Walden et al. (2003) studied DD, blowing snow, and cloud precipitation in winter, at SPS, by collecting crystals on slides and analyzing them using microphotography. In their study, columns with an average length of 60 μm and plates with an average diameter of 30 μm were found in DD. The direct observation of ice precipitation on the plateau was typically carried out by means of formvar replicas and/or microphotography, but these techniques take time, are difficult to implement throughout the year and are necessarily limited to short field campaigns and samples of very limited size. Designing automatic instruments for the continuous, photographic study of precipitation in such a harsh environment necessarily require several compromises between the high resolution of microphotography and the robustness of outdoor optical instruments such as disdrometers. Lawson et al. (2006) worked at SPS, in summer, using innovative Cloud Particle Imagers (CPIs), which replaced formvar replicas. This technique allowed the automatic analysis of around 700,000 DD crystal images in terms of caliper size, aspect ratio and other shape parameters. An automatic classification software, based on shape parameters, was used to categorize the images into nine simplified classes: small plates and spheroids, columns, thick plates, plates, budding rosettes, rosettes, complex with side planes, irregulars.

Concordia International Station, located on the Dome-C (DC, 75°S,123°E, 3220 m above sea level) is a special location to test new instruments for precipitation studies. Surface temperatures seldom exceed -25°C in summer, whereas winter temperatures can reach -85°C. The 3 m average wind speed is 3 ms^{-1} for Aristidi (2005) and 4.5 ms^{-1} (hourly-averaged) for Argentini et al. (2014). The strongest winds (up to 15 ms^{-1}, hourly-averaged) blow from the

86 continental regions. These winds are due to gravity flows from the inner plateau regions south of Dome C, and are more often
87 observed during the winter, especially in coincidence with warming events. The circulation at the surface during the summer
88 is affected, especially in daytime, by the synoptic circulation. In summer the wind speed oscillates during the day, with values
89 increasing (by a few ms^{-1}) in the afternoon, when a convective layer develops, leading to the increase of the wind speed
90 (Argentini et al.,2014). Relative humidity relative to ice is typically around 55-85% (Genthon et al., 2022). In these conditions,
91 precipitation of ice crystals can be studied by simply collecting them on horizontal surfaces. This is done at DC by hand,
92 starting in 2008, collecting precipitation on flat surfaces ("benches") and visually inspecting it. This analysis is restricted to
93 one observation per day, a rate that is difficult to increase, especially in winter. The analysis of these samples is also time-
94 consuming and often subject to biases due to ice re-processing and sublimation, hoar formation, and subjective judgement of
95 the shape and relative abundance of ice particles. Schlosser et. al (2017) relied on this manual observation and classification
96 of ice particles in his analysis of precipitation isotope data at DC. They classified the ice grains into diamond dust, drifting
97 snow, snow and frost (hoar). The prevalence of hoar in the observed daily precipitation record (with temperatures below -
98 50°C) indicates the limitations of this manual technique if detailed information on DC precipitation particles is desired.
99   Detailed work was carried out in DC on a few individual DD and cloud precipitation crystal replicas by means of SEM electron
100 microscopy by Santachiara et al. (2016). They also analyzed very small particles (10-50 μm), in a size range inaccessible to
101 ordinary   optical   methods.
102 The purpose of developing ICE-CAMERA was to fill a gap in precipitation monitoring at Concordia with a robust instrument
103 capable of monitoring with continuity, all-year round, habit and size of ice particles in precipitation, while avoiding some of
104 the problems associated with the visual inspection of precipitation. This was achieved through the combined development of
105 robust camera equipment and machine learning techniques for sizing and classifying ice crystals.
106
107

108 **2. The instrument.**
109 **2.1 Overview of ICE-CAMERA.**
110 ICE-CAMERA is a flatbed scanner (Zheleznyak et al, 2015), whose operating principle is the same as that of ordinary
111 flatbed scanners in offices. In the case of ICE-CAMERA, it specially designed for observing polar precipitation in the harsh
112 environmental conditions of Concordia station (Fig. 1). Within this work, the term "precipitation" will include both
113 "diamond dust" and cloud precipitation. The 'Deposition Surface' (DS) is defined as the horizontal, glass surface of the
114 instrument facing the sky and collecting precipitation.
115
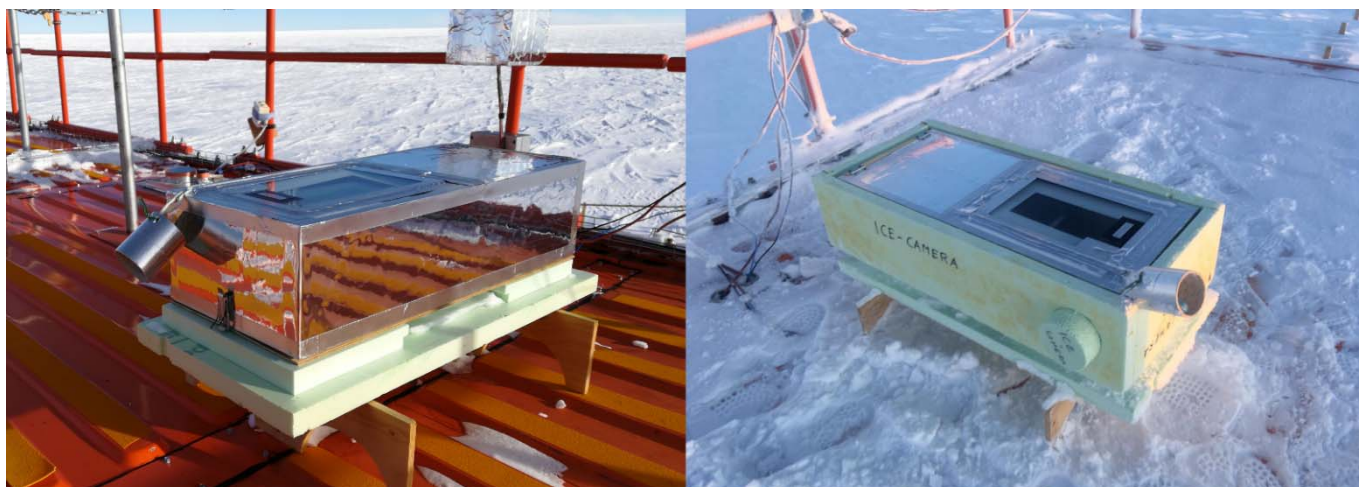
116
117 **Fig. 1: ICE-CAMERA with its summer sun-shield (left) and with the winter coat (right).**
118

119

120   The principle is simple: at the low temperatures and low wind speeds typically encountered at DC, precipitation falling on a

121 horizontal glass surface accumulates with time until it sublimates, leaving enough time for scanning the DS for counting and

122 measuring individual ice particles. The DS is the external surface of a special glass with electric heating (2.7). A second sheet

123 of glass together with the DS glass creates a double glass window that isolates the DS from the heated parts of the instrument

124 (Figs.2, 3). The scanning, like in ordinary flatbed scanners, is performed by means of a line-scan camera (Sect.2.2). moved by

125 a motorized scan sledge, and looking up at the DS through a 45° mirror (Fig. 2). The focus of the camera is adjusted by a

126 small motorized focusing sledge moving the 45° mirror (Sect.2.3). During the scan, the image is sent to the PC, located inside

127 the shelter.

128 After a complete scan of the DS, the glass is heated and the precipitation sublimated (section 2.7). Once cooled down, the

129 clean SD begins to accumulate new particles. This cycle takes place every hour. After each image acquisition, the MATLAB

130 image processing code is called to process the DS image, and a summary-image containing only segmented particles (if

131 present) is stored for post-processing. (Sect. 4.1.3). Every particle is also automatically measured through image processing

132 (Sect. 4.1) and classified through machine learning (Sect.4.2). Individual particle data are stored in rows in a text file, along

133 with weather and housekeeping data, for post-processing and statistical analysis.

134
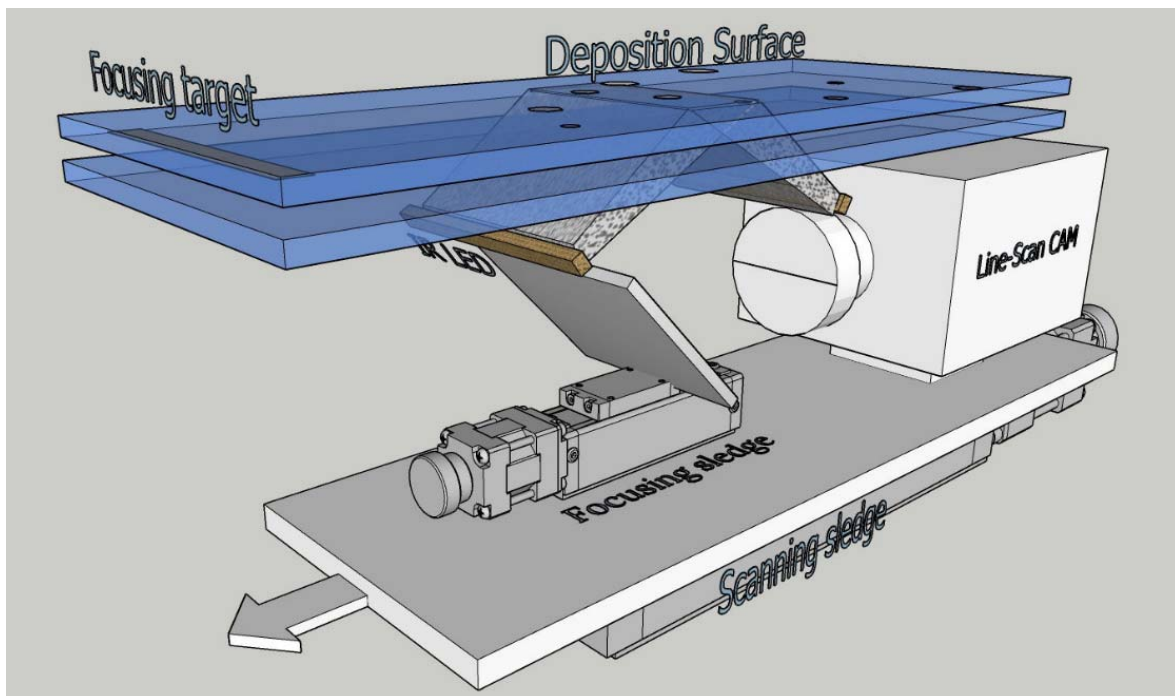
135

136   **Fig. 2: ICE-CAMERA basics: the scan sledge moves the image-acquisition line along the deposition surface. The focusing sledge**

137 **adjusts the focus.**

138

139 All basic operations of ICE-CAMERA, (with the exception of CAM acquisition) are driven by a custom microprocessor

140 (Microchip PIC) logic board (Fig. 3). The same PIC board reads the housekeeping temperature sensors (attached to the DS

141 and placed inside and outside the instrument), drives the stepper motors of the sledges as well as pumps and fans. The PIC

142 Board communicates with the main computer (located inside the shelter) through RS232. NI Labview software controls image

143 acquisition, reads maintenance data, and monitors PIC operations along the RS232 line. The line-scan camera communicates

144 with the PC via Gigabit Ethernet.

145 The instrument is placed outdoor, on the roof of the "Physique" shelter, approximately 6 m above the ground.

146 ICE-CAMERA was first installed in Concordia in 2012, but replaced in 2014 with its improved version, described here.

147 From then on, the instrument works year-round to produce precipitation data, every hour. Standard meteorological data are

148 automatically obtained from local weather station AWS MILOS 520.

149

150
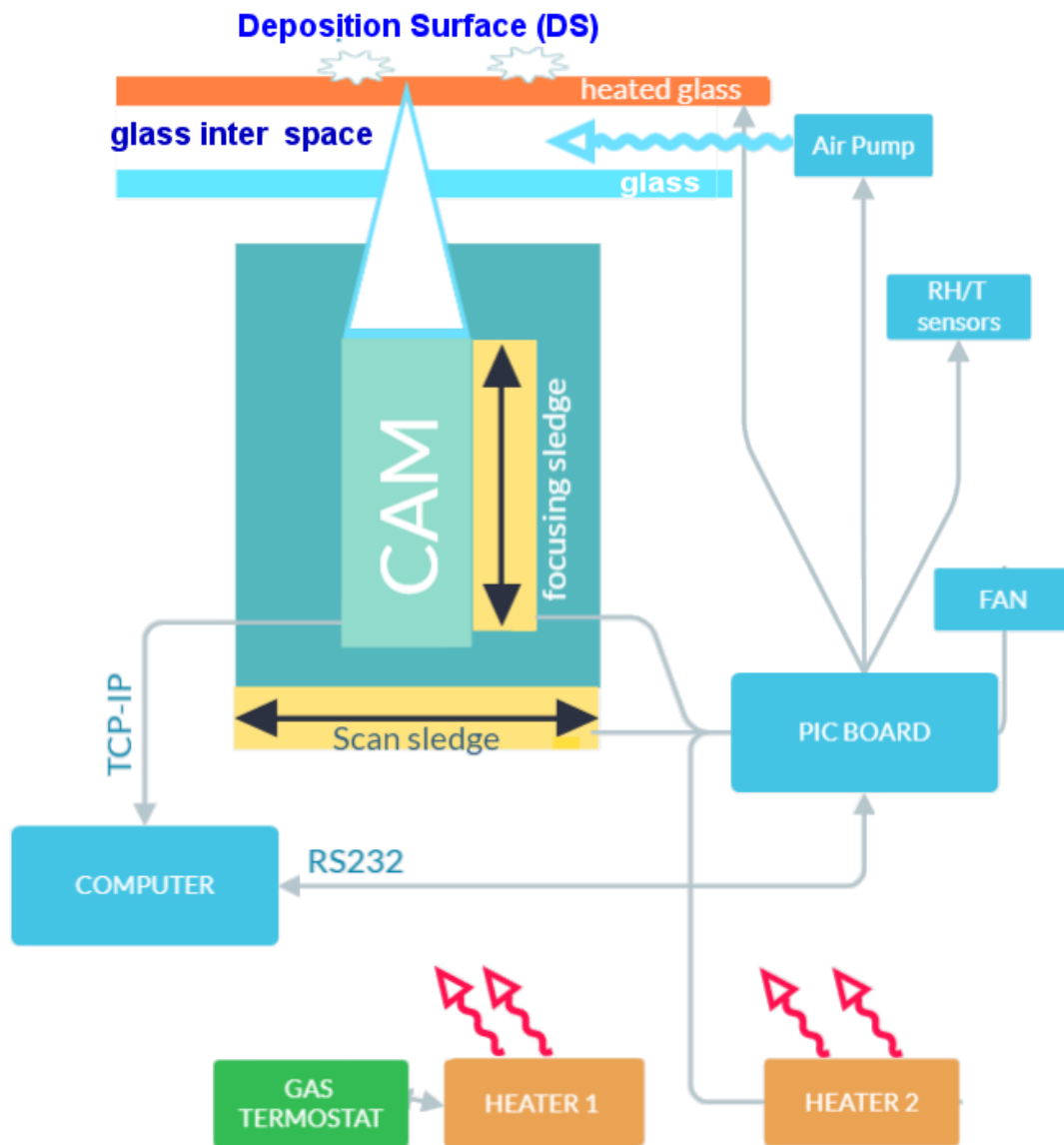
151

152

153 **Fig. 3: Basic schematics of the instrument**

154

155 **2.2 The line scan Camera.**

156 A linear scanning GigE Vision monochrome camera (Schafter-Kirchoff SK7500VTF-XB (52.5 mm sensor, 7500 pixels,

157 7x7μm pixels, 8.2kHz line frequency), equipped with a 1:1 macro lens (APO-Rodagon D1X, f5.6) is used for the acquisition.

158 The optics were designed by Schafter-Kirchoff in order to have a resolution equivalent to the 7μm pixel size. The 45 deg

159 mirror is used to look upward. The illumination is ensured by 850 nm LEDs. A colour filter (Schott RG715, 800-1000 nm

160 band-pass) was used on the CAM lens, in order to have a fully solar blind instrument. The line-scan camera assembly is moved,

161 hourly, by a motorized sledge at a speed of 8 mm s^{-1} in order to scan the rectangular DS (55x200 mm), located at the center

162 of the window. The final image is 7500*30000 pixel, 12 bits, monochrome. A fine calibration of the actual pixel size of the

163 DS image was achieved by scanning a calibrated grid (0.1mm spacing) placed on the DS. This is necessary because the

164 effective resolution of the image produced by the moving linear camera along the sledge direction depends on how fast the

165 sledge moves. After the correction of this effect, the image pixel size resulted in 6.97 x 6.9 μm, which was extremely close to

166   the simulated size of 7x7 µm.. For the Nyquist sampling theorem, details less than 14 µm cannot be detected in the image

167   (under optimal focusing conditions). This resolution is enough, for example, for the observation of the hexagonal edges of the

168   smallest plates detected by the instrument.

169   2.3 The Focusing.

170   In working conditions, the focal depth is ±0.5 mm. A preliminary and accurate alignment of the motorized sledge plane to

171   the DS ensures uniformity of focus across the DS at room temperature. A motorized focusing sledge, moving the bending

172   mirror, allows to adjust the focus in operating conditions (Fig. 2). As ICE-CAMERA works outdoor at DC, it can

173   experience a broad internal temperature range, from +5°C in summer to -45°C in winter, with quite large temperature

174   gradients across the structure. Thermal expansion and changes in optical refractive indexes result in unpredictable changes in

175   the focal plane. The correction of the focus is thus automatically performed, every 6 hours, by bringing the measuring sledge

176   outside the DS, where a focusing spot (a sandpaper strip) is glued to the window (Fig. 4).

177
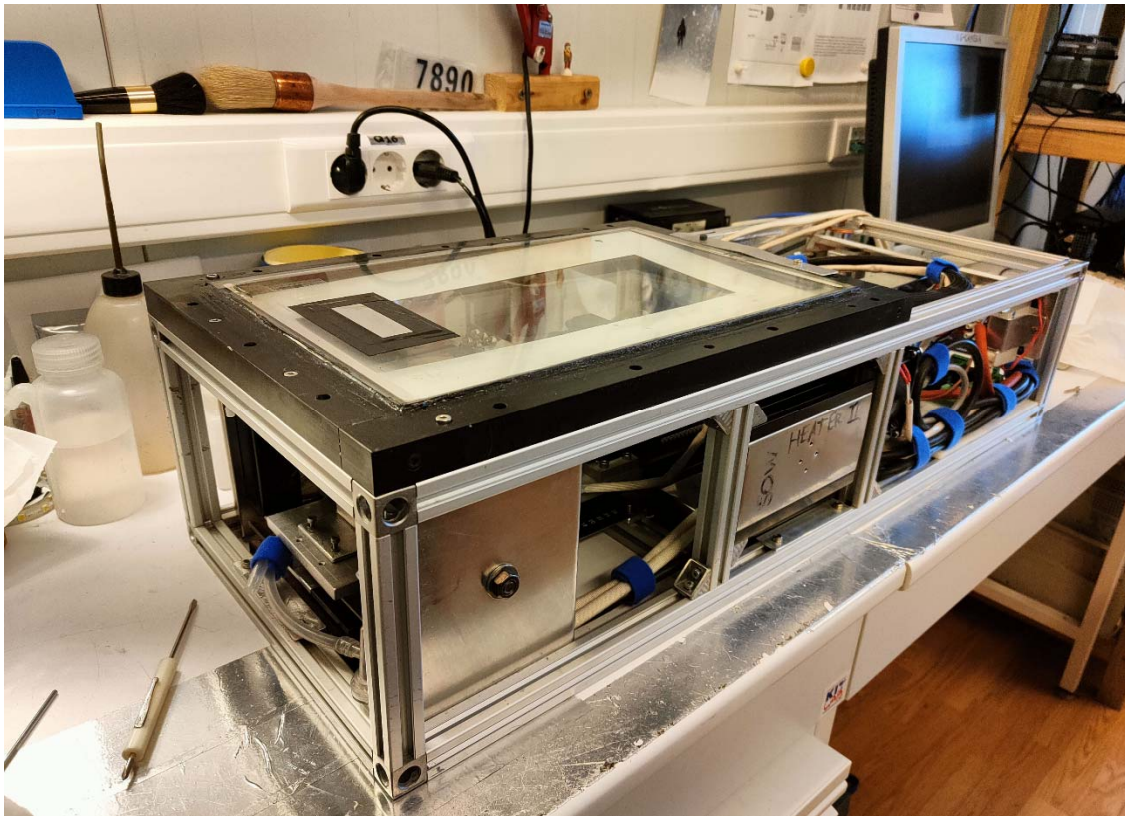
178

179   **Fig. 4: ICE-CAMERA out-of-the-box. The focus target if fixed onto the DS.**

180

181   The porous structure of the sandpaper has a length-scale of the order of 0.1 mm, comparable with the size of the measured

182   ice particles. While calibrating, the focusing sledge is moved by ±2 mm around the actual position in 0.25 mm steps.

183   Successive images of the sandpaper are taken and their contrast (defined as the standard deviation of the intensity of the

184   pixels) is measured. After a Gaussian-fit of the contrast as a function of defocusing (Fig. 5), the position corresponding to

185   the maximum contrast is obtained, and the mirror sledge is moved into that position. The typical focal spot adjustment

186   between two consecutive calibrations if 0-0.25 mm. The calibration takes approximately 5 minutes. For this reason, it is not

187   done after each measurement, so as to save PC resources for data processing.

188
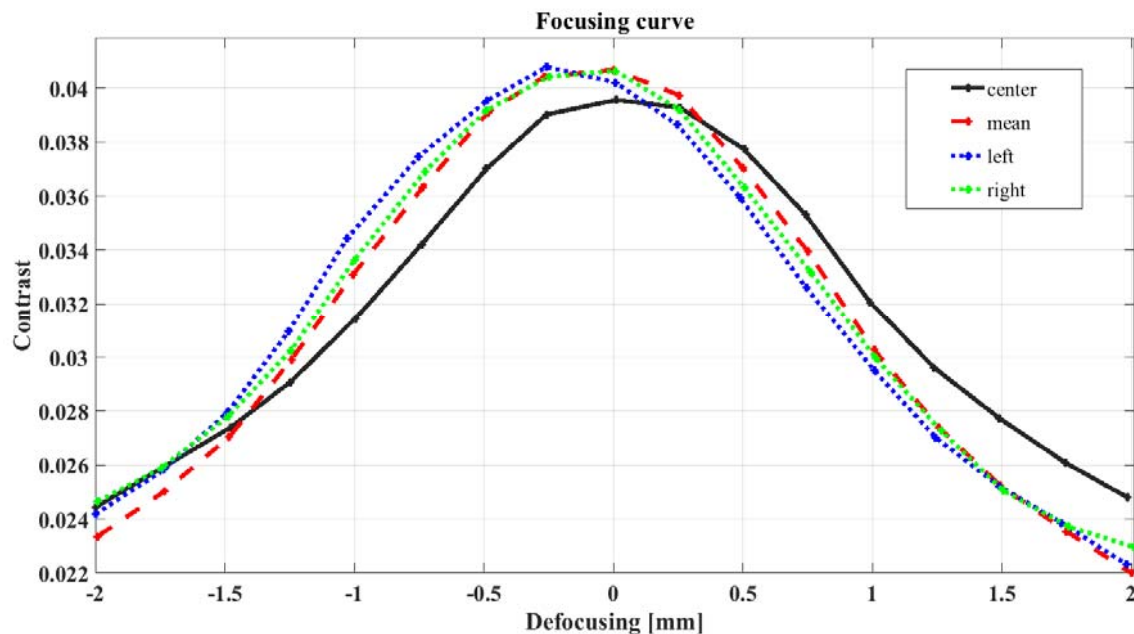
Fig. 5: Typical focus calibration: Contrast is calculated in three sectors of the image: center, left and right. The contrast throughout the image is also displayed (red). The slight difference in focus (0.2mm) between the center of the image and the side wings is a normal lens effect.

2.4 Illumination.

Lighting is supplied by two 850 nm LED (TSHG6200) strips. Both arrays illuminate the scan line symmetrically and approximately 45° from the optic axis in order to minimize multiple reflections in the double glass and within the camera lens. Infrared illumination was chosen in order to work in solar-blind conditions. This is particularly important, as the linear scanning camera always looks upward, to the sky. The uniformity of lighting along the linear CCD image was tested by taking an image of the same sandpaper used in the focus. The intensity profile along the CCD image was measured, and the intensity of the LEDs eventually changed to have a final intensity uniformity across the entire frame of less than 15%.

2.5 The Deposition Surface (DS).

The DS is the external surface of a 10 mm thick, electrically-heated glass (E-GLAS, Saint-Gobain). The glass is a sandwich with an electrically conductive layer pressed between two usual glass sheets. This glass is transparent at 850 nm, and can be electrically heated with 45 V ac, 95 W . A second, 2 mm thick, optically graded glass sheet (an ordinary flatbed scanner optical glass), placed 13 mm under the DS, makes up with the DS a double glass. This arrangement is necessary in order to keep the DS thermally insulated from the heated, interior of the instrument. A thermocouple is attached to the DS, while other thermocouples monitor double glass inter-space temperatures. A temperature of (at least) 3 °C above air temperature is enough to prevent, in DC, the formation of frost on surfaces in any season, as suggested by the work of Tremblin et al., (2011). In ICE-CAMERA, the temperature of the DS is usually 4 to 5°C above room temperature, which keeps the DS free of frost in all seasons (Fig. 6).

213

Fig. 6:   ICECAMERA at -70°C, Concordia station winter: the DS if free of frost

214

215

216

217

218 During the sublimation period (Sect.2.7), ambient air is pumped for five minutes by means of a 3.5 l m⁻¹ miniature pump

219 through the double glass inter space, in order to keep the internal surfaces of the double glass always free of frost. Using

220 inert gases such as argon in the double glass space for the same purpose proved unsuccessful in Concordia at the extremely

221 low winter temperatures. In order to avoid the eventual accumulation of wind-drifted snow, the DS has no walls or obstacles

222 all around. Furthermore, the instrument is located on the roof of a shelter, almost 6 meters above the ground, an altitude

223 where blowing snow is not normally important at Concordia. Libois et al. (2014) identify drifting snow events at Dome C

224 when the 10-m wind speed exceeds 7 m s^{-1}. Assuming a logarithmic wind speed profile between the surface and 10-m and

225 an aerodynamic roughness length value of 1 mm (Vignon et al., 2016), this corresponds to a wind speed threshold value of 5

226 m s^{-1} at 6 m above the ground. Winds below this threshold (near the annual average wind speed in DC) are not expected to

227 carry blowing snow to the DS. In addition, blowing snow impacts the flat horizontal and smooth DS at very small angles,

228 with a very limited chance of sticking to it. As a consequence, ice particles collected on the DS can be considered

229 representative of precipitation. In case of strong winds, not only the attachment of blowing snow to the DS is very low, but

230 also the collection of eventual precipitation is reduced. Since DS is warmer than air, there is no secondary growth in

231 deposited ice. Instead, the partial sublimation of ice particles before scanning could not be excluded, especially in summer.

232 This topic needs additional field work and will be modelled in Sect. 3.2.

233

234 **2.6 The thermal control.**

235 The temperatures measured by the ICE-CAMERA sensors are continuously transferred to the computer. The NI-Labview

236 software controls the internal temperature of ICE-CAMERA above -40°C (by driving the 200W, ventilated air heater "Heater

237 2" of Fig. 3), and the DS temperature always under -5° (by eventually disabling the "heated glass" of Fig.3). These conditions

238 are maintained throughout the year during every phase of the measuring cycle. An independent 200W thermostat ("Heater 1"

239 in Fig. 3) provides emergency temperature control in case of computer or PIC board failure. After a black-out, when the power

240 is restored, a timer is used to heat the inside of the instrument before turning on the electronics. This is important at Concordia

241 to   prevent   damage   to   standard   electronics   with   typical   operating   temperatures   of   -40°C.

242 In winter, a 40 mm thick Styrofoam coat is added around the instrument for increasing thermal insulation, whereas in summer

243   a Mylar sunscreen prevents overheating of the instrument and allows keeping the DS below -5°C in the warmest days (Fig.

244   1). Additionally, in warm weather, outdoor air is carried inside the box with a tangential fan, for better cooling of the

245   instrument. The DS temperature (without heating applied to DS glass) is on the average 4 to 5°C above the air temperature.

246

247   **2.7 Sublimation-deposition cycle.**

248   After an entire scan of the DS, electricity is applied to the DS glass to sublimate the particles. The heating rate of the DS

249   depends primarily on the electrical power applied to the glass and its thermal constant (approximately 0.8 W m^{-1} K^{-1}) , and

250   secondarily on the wind speed. An indoor test (Fig. 7), showed a heating of rate of 2.5°C min^{-1}, and a cooling rate of 1 °C

251   min^{-1}.

252
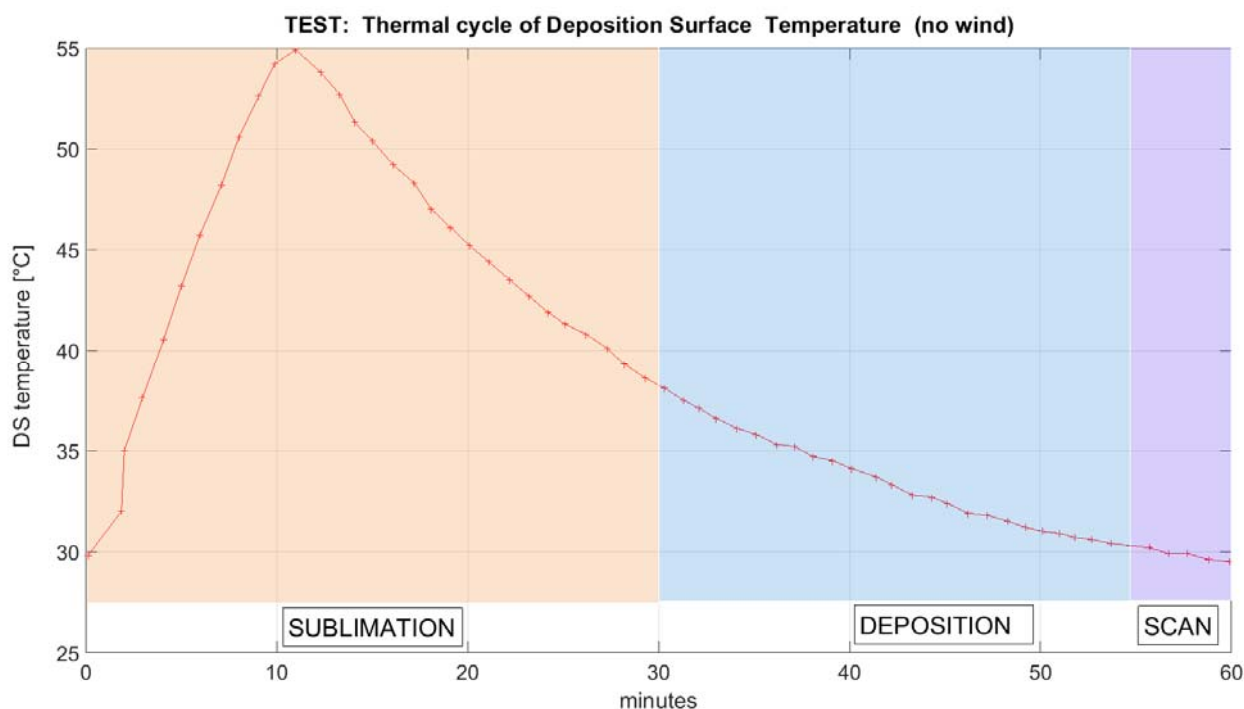
253   **Fig. 7 : Indoor test of DS heating-cooling within a 60 min cycle. For reasons of simplicity, the periods of sublimation and**

254   **deposition are well separated..**

255

256   The cooling rate is at most only about 50% of the heating rate. Cooling is passive through heat transfer to ambient air, with a

257   heat transfer coefficient of approximately k=0.024 W m-1 K-1 in still air. k increases with radiation cooling, convection and

258   wind. During glass heating, heat is quickly transferred to the DS from the electrically heated inner layer, while during

259   cooling the heat transfers from the DS to the air occurs slowly, with a thermal constant k. This explains the asymmetrical

260   curve of Fig.7.

261   Outdoor tests carried out in summer at DC (-30°C air temperature) showed a heating rate of 3 °C min^{-1} in still air, 2.5 °C

262   min^{-1} with 2.5 m s^{-1} wind speed, and 1.8 °C min^{-1} with 5 m s^{-1} wind speed. In all cases, the cooling rate was approximately

263   1.5 °C min^{-1}.

264   An outdoor sublimation test (-30°C air temperature, RH=60%, wind speed <3 m s^{-1}) performed with snow manually spread

265   on the DS showed that, after applying heating for 10 minutes (up to a DS temperature of -8°C) the sublimation of the

266   majority of particles (diameter<1000 μm) was complete within 20 minutes after turning off the heating, with just a few big

267   grains (initial diameter>1000 μm) still present after 30 minutes.

268   After these tests, the glass heating period was set at 10 minutes (the heating is stopped anyway if the DS temperature exceeds

269   -5°C to avoid melting of the ice in summer). At the peak of the sublimation period, DS resulted warmer than air of about dT

= 20°C. Once the heater is turned off, and after a cooling time of approximately 20 minutes, the DS temperature comes back to be warmer than the air by only 4-5°C. At this point the "sublimation period" (of approximately 30 minutes) is considered complete, and ice particles start accumulating again on the DS, with no relevant sublimation, i.e. the "deposition period" begins (as sketched in fig.7 for the indoor test). At the end of the deposition period, a scan of the DS is carried out, for a duration of one minute. If no ice particles were detected on the previous scan, the DS heater is not applied, sublimation is not needed. The effective deposition period depends on the temperature, wind and exposure to the sun in summer. This uncertainty, combined with occasional wind removal and particulate sublimation (Sect. 3.2) during the deposition period, prevents the use of ICE-CAMERA for rigorous quantitative precipitation studies.

DS surface temperature is actually measured by using a small thermocouple. This measurement implies great uncertainties due to the radiant warming of the sensor in summer and the difficult thermal coupling with the glass surface. A non-contact measurement of DS temperature by means of IR sensors would also be uneffective in winter conditions.

3. Ice particles and the deposition surface.

3.1 Adhesion of ice particles on the DS.

The adhesion of ice crystals to the smooth DS is caused by two principal reasons: Van der Waals and electrostatic forces. Eidevåg et al (2020) studied the adhesion of dry snow particles after 90° impact to different wall materials (gravity is a minor force in this application, and therefore their work applies to any wall orientation). They considered models for normal direction, tangential sliding, and tangential rolling that account for the adhesive interaction of spherical ice particles (25-275 μm diameter) and their aggregates. The Johnson-Kendall-Roberts (JKR) model for adhesion was used. Their findings showed that the maximum normal velocity at which spherical ice particles adhere to a glass surface (critical stick velocity) decreases with decreasing particle diameter. Spherical particles of 100 μm would adhere for speeds less than 0.02 m s^{-1}. The numerical method of Eidevåg et al (2020) has been applied in the present work to compute the critical sticking velocity of spherical ice particles up to 1000 μm diameter. The sedimentation velocity of ice crystals up to 1000 μm was also calculated using the formulation of Böhm (1989) for DC conditions (Tair=-50°C , air density=1.03 kg m^{-3}, dynamic viscosity= 1.45E-5 Pa s). Particles impacting on the DS with a sedimentation velocity lower than the critical sticking velocity are immediately captured with 100% efficiency by Van der Waals forces. The simulation shows that only spherical particles smaller than 50 μm in diameter fall on the DS with a speed smaller than the critical stick velocity, and thus stick immediately. This result does not change with the different forms of particles, as for these sizes the speed of sedimentation is close to that of Stokes. Particles above 50 μm in diameter have an excess of kinetic energy to bind effectively immediately on the DS. However, the impact surface (DS) is horizontal, so that the excess kinetic energy is rapidly dissipated in one or more vertical rebounds, until the critical sticking velocity is achieved (Chokshi et al.,1993). So the adherence of ice crystals to the DS could also be explained by the forces of Van der Waals alone. Ryzhkin and Petrenko (1997) showed that static charges, naturally transported by ice crystals, increase adhesion. The electrostatic interaction between the ice and the surface is significantly stronger than the van der Waals forces at distances greater than the inter-molecular forces. Electrostatic forces are therefore expected to significantly improve the adhesion of large ice particles to the DS. Once attached to the DS, the weak winds generally observed at DC cannot detach the particles from the DS. Particulates are protected by the boundary layer (BL) that forms on the DS. The 99% thickness of the laminar BL (Blasius solution) at the centre of the DS (0.15 m distance from the glass edge) is expected to be 7 mm at -50°C with a wind speed of 1 m s^{-1}, decreasing to 2 mm at 10 m s^{-1}. As a result, the particles deposited on the DS are protected against the wind.

3.2 Sublimation of ice particles.

The DS is always warmer than the surrounding air. This is necessary to eliminate hoar, enabling the device to be used in all DC conditions. The undesirable effect is the accelerated natural sublimation of deposited particles. A wide range of experimental and theoretical research efforts has characterized the effects of temperature and super-saturation on ice crystal growth rates and morphology under conditions relevant to atmospheric processes (for example Lamb and Hobbs, 1971; Libbrecht, 2005; Libbrecht, 2017). The wide variety of ice crystals found in nature has sparked an interest. Sublimation was sometimes regarded either as the opposite process, or a less intriguing process, and was less visited in lab studies. Nelson,(1988) sublimated numerous, 100 μm diameter plate crystals (0.1°C>T>-18°C, 0.05% to 5% sub-saturation) showing that the crystals first lost sharp edges, and finally evolved into spheroidal particles, and the aspect ratio remained almost constant. The sublimation rates were accurately predicted by the diffusion equation with the surface vapour density at the equilibrium value for a uniform surface temperature. The sublimating crystal reaches a self-preserving shape that is one of the shape preserving solutions of the diffusion equation. Ham (1959) showed that ellipsoids and thus spheroids preserve shape during growth and sublimation if the grain surface has a uniform temperature. Jambon-Puillet et al.(2018) also showed experimentally and theoretically that sublimation first smooths out regions of sharp curvature, leading to an ellipsoid. The second stage is the sublimation of the self preserved ellipsoid shape. The entire process may be modelled as a vapour diffusion problem, mathematically equivalent to the resolution of the electrical potential around a charged conductor. Using this analogy, they provided a mathematical method for simulating the sublimation of the ice particle. The sublimation of the ellipsoid turned out mathematically simple, and their method was adopted in this work to numerically simulate the second stage of sublimation of ICE-CAMERA particles.

Monodispersed oblate spheroids with an aspect ratio (AR) of 5, in thermal equilibrium with the DS, were assumed in the simulations as a surrogate for ice plates. The two major spheroid axes coincide with the «diameter» of the oblate spheroid, D. In the model, D, DS temperature, air temperature and relative humidity with respect to ice (RHair) can be changed. The sublimation time required for full sublimation of a spheroidal ice particle was computed. As sublimation accelerates when the particle is going to vanish, the time necessary for the complete sublimation is only slightly larger than the time necessary to reduce the particle to the minimum particle size (D=60 μm) accepted by ICE-CAMERA image processing. The simulations assume that the preliminary sublimation of the high-curvature parts of the particle (sharp edges, corners, surface irregularities) was already completed, so that the calculated time of sublimation must be considered as a lower limit for real-world crystals, and probably almost one half of the overall duration of sublimation (Jambon-Puillet et al.,2018). Simulations also assume the thermal equilibrium between the particle and DS, a condition which is not necessarily satisfied on the thermally insulating glass surface of the DS. Figure 8a shows the total sublimation time with the DS heated dT=+20°C above air temperature (sublimation period). The humidity resulted irrelevant in this case, and only results for 70% RHair are shown. Results show that at -30°C air temperature (summer conditions in DC) complete sublimation can occur within a few minutes after attaining the DS sublimation temperature, for all particle sizes up to 1 mm. At lower air temperatures, the sublimation time increases: at -70 °C (winter temperature in DC), particles smaller than 100 μm in diameter still disappear within 10 minutes, while larger particles can survive along the sublimation period. Simulations showed that, at -70 °C, dT should be increased to dT=60°C in order to ensure the complete sublimation of ice particles up to 1 mm diameter during the sublimation period. This is actually not possible with the electric heated glass adopted, but could probably be achieved by microwave heating.
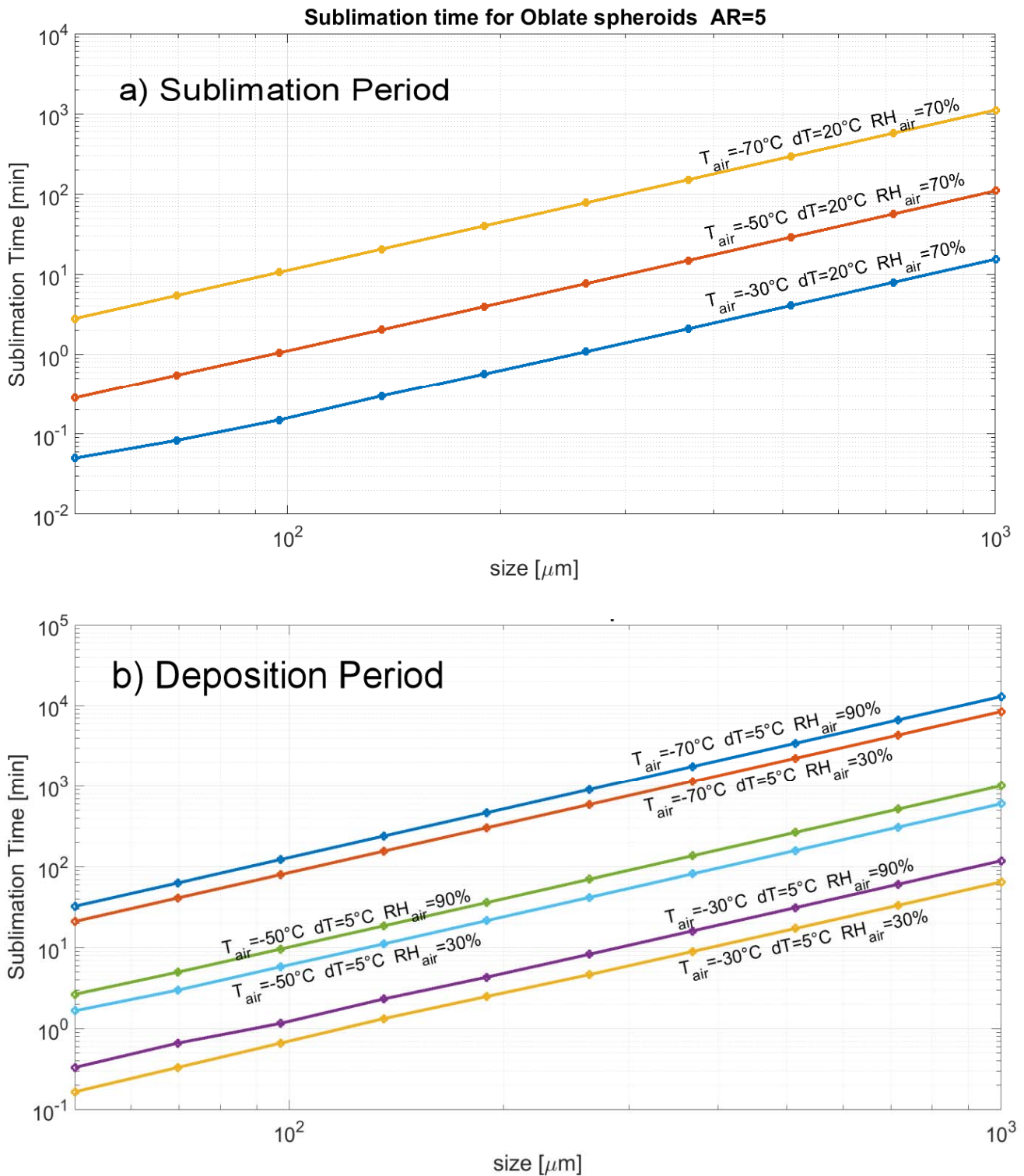
Fig. 8: Sublimation time of monodisperse oblate spheroids at varying air temperatures, with a) dT = 20°C (sublimation period) and b) dT=5°C (deposition period).

After the sublimation period, most of the particles previously collected on the DS are sublimated, and a new deposition period begins. Even during this period, sublimation still acts on ice particles, albeit slowly. Figure 8b shows the sublimation time expected for monodisperse spheroids during the deposition period. The DS was considered 5 °C hotter than air. As shown, during the deposition period the relative humidity of air also plays a role, even if secondary. In summer (T_{air}=-30°C), sublimation can take less than a minute for particles smaller than 100 μm and ten minutes for 300 μm particles. During winter (T_{air} = -70°C), all particles are expected to survive through the deposition period. As a rule-of-the-thumb, simulation showed

361 that working with dT=+5°C resulted in an increase of the rate of sublimation by a factor 2-3 compared with a DS in thermal

362 equilibrium with ambient air (dT=0) for the whole range of air temperatures and RHair shown in Fig. 8b.

363 Results of Fig.8b show that the effective lower limit of ICE-CAMERA particle detection is not limited solely to the resolution

364 of the optical system and/or image processing software. In summer, particles smaller than 100 μm may be decimated during

365 deposition, unless they fall just before scanning. Such small particles dominate diamond dust events. As a result, ICE-

366 CAMERA, during the summer period, is best suited to the study of cloud precipitation. Nevertheless, visual screening of ICE-

367 CAMERA images showed only a limited number of small particles revealing signs of partial sublimation, such as rounded

368 corners, smooth edges, or a spheroidal appearance. Some small plates (observed mainly in winter, when sublimation during

369 the deposition period is very slow) showed smoothed corners, but it is not clear if this was induced by sublimation or is a

370 natural feature of these ice grains. Also, even in summer, small DD particles such as plates (with no signs of edge smoothing)

371 were normally observed (Sec.5.2). It is probable that most particles (other than, probably, pristine plates) never achieve thermal

372 equilibrium with the DS glass, and that the results of Fig.8 should be considered as the worst case. Also, the sublimation of

373 the high-curvature parts of the particle prior to assuming the spheroidal form (Jambon-Puillet et al.,2018) could take much

374 more time than the sublimation time calculated here for the spheroid. A series of consecutive DS scans at fixed air temperatures

375 is needed to measure the effective sublimation rate of small particles in deposition conditions (dT=+5°C).

376  When a polydisperse particle population is deposited on the DS instead of monodisperse particles, a more complicated

377 sublimation picture arises, because small spheroidal particles, shrinking, are continuously replaced in the size distribution by

378 sublimating, initially bigger ones. An initial uniform particle size distribution (PSD) of the oblate spheroids (AR=5) was

379 assumed with diameters between D=1 and 2000 μm for the simulations. The evolution over time (1 sec resolution) of the PSD

380 was calculated (Fig. 9) in terms of particle survival (the ratio between the actual number of particles in a certain size bin and

381 the initial number in the same bin). No vapour competition between ice particles was taken into consideration in the

382 simulations. Results are similar to those of monodisperse particles (Fig. 8), with a slightly longer time of sublimation for

383 polydisperse particles compared to monodisperse particles of the same size. Results for an air temperature of -70°C confirm

384 that most particles larger than 500 μm survive, throughout the DS sublimation period (dT = 20°C), longer than 30 minutes.

385 This means that sublimating by heating the glass is quite inefficient for large particles in winter. During the deposition period,

386 at -70°C losses for sublimation are scarce and limited to particles smaller than 200 μm. Consequently, double counting of the

387 same particle (D>500 μm) is possible in two consecutive ICE-CAMERA scans in the cold DC winter. At -30°C air temperature

388 (summer) the heating of the DS with dT=20°C leads to the sublimation of most particles up to 2 mm diameter within 5 minutes.

389 On the other side, during the deposition period particles smaller than 500 μm can undergo sublimation over a period of just 10

390 minutes in summer, thus limiting the effective period of deposition before a scan. As with monodisperse particles, this

391 introduces bias in the summer because many small particles (typical of DD) can be removed before they are measured.
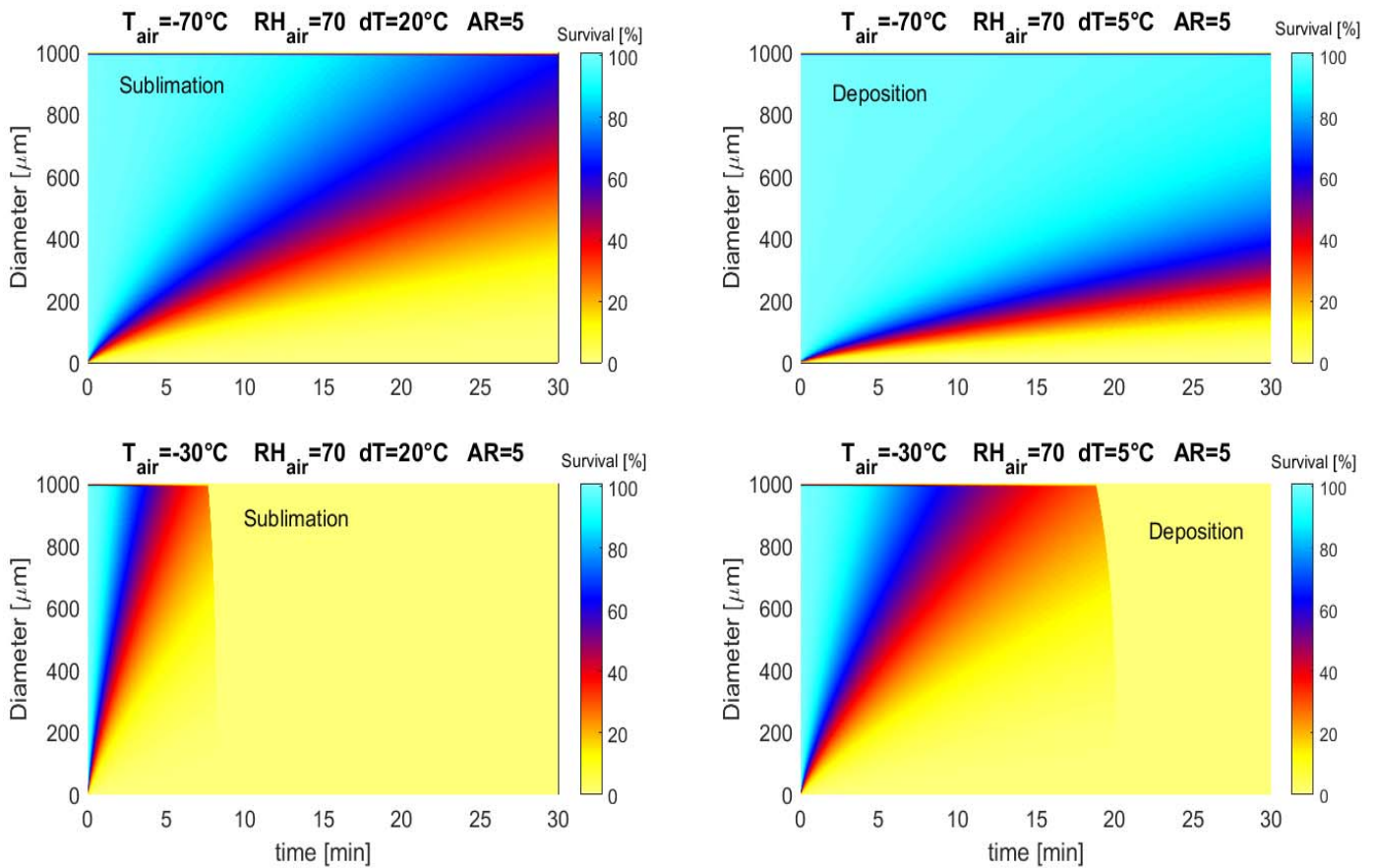
Fig.9: Evolution of a originally uniform PSD of ice spheroids (D=0-2000 μm, AR=5) under different atmospheric conditions. (RHair is a secondary factor affecting the results, shown here for RH=70%). Left: sublimation period; right: deposition period. Top: winter, bottom: summer.

Even if these results could be disappointing for interpreting ICE-CAMERA data, the same problems affect the actual method of observing precipitation in DC: collecting and observing (every 24 hours) the ice particles deposited on flat surfaces ('benches') is affected by the same problem as collecting particles on the ICE-CAMERA DS with dT=0. Fluctuations in relative humidity over 24 hours result in sublimation and regrowth of particles on the "benches" in an almost unpredictable manner. Fig. 10 shows the expected sublimation time for particles (with the same PSD of Fig. 9) placed on 'benches' (or ICE-CAMERA DS) in equilibrium with air (dT=0) for extreme, sub-saturated conditions: winter Tair=-70° (RHair=30% and 99%), and summer Tair=-30 (RHair=30% and 99%). The PSD evolution is computed with a resolution of 1 sec for a total period of 6 hours. The results show that sublimation also works in winter and with almost saturated air (99% RHair), leading to a complete loss of small particles (D<200 μm) in a few hours. In summer conditions and 30% RHair sublimation happens much more quickly, with the disappearance of all particles up to 2000 μm in 30 minutes. With RHair=99%, sublimation removes all particles in just a few hours in summer. In presence of wind and dry air, sublimation rate could even increase, as observed by Grazioli et al., 2017 in coastal areas. These simulations all refer to sub-saturated conditions: in the case of a 'bench' in thermal equilibrium with super-saturated air, hoar form on the surface, with a possible confusion with precipitation.

410
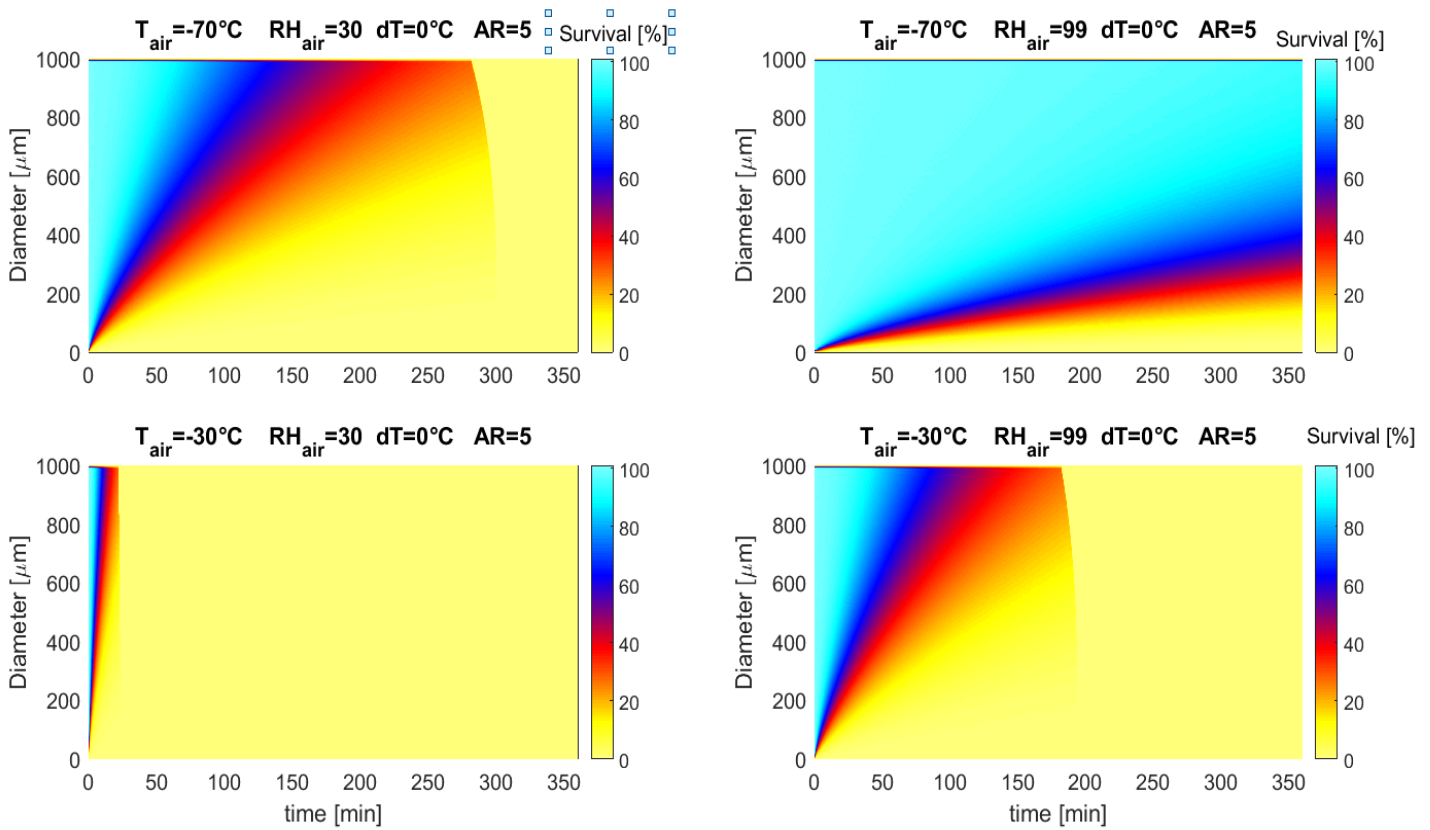
Fig.10: Evolution of a originally uniform PSD of ice spheroids (D=0-2000 µm, AR=5) under different atmospheric

412 **conditions. The DS (or 'bench') is in thermal equilibrium with air (dT=0). Top: winter, bottom: summer**

413

414

415 **4. Data processing.**

416

417 **4.1 Image processing.**

418 ICE-CAMERA is not just designed to take photographs of ice particles, but to provide automatic morphometry and

419 classification of polar precipitation. This was accomplished through the use of image processing and machine learning

420 techniques. The process is divided into two parts: segmentation and measuring, and classification of ice crystals.

421

422 **4.1.1 Image segmentation and measurement of ice particles.**

423 After acquisition, the raw ICE-CAMERA scans are segmented, using MATLAB software, to isolate all detected particles. The

424 process follows the workflow of Fig. 11. Refer to Pratt (2007) for image-processing nomenclature, to Walton, 1948 for Feret

425 measurement, to Russ and Brent Neal (2017) for the nomenclature of standard shape parameters such as Eccentricity, Euler

426 Number, circularity, roundness, solidity, compactness, form factor, and number of skeletal branches. The normalized central

427 moments f1...f7 were also computed as described by Hu, (1962).

428 The Aspect Ratio (AR) is defined as Feret's length/ Feret's width. The Feret-box surface-equivalent diameter (Df) is defined

429 as the diameter of the circle of the same area as the Feret bounding box, while the surface-equivalent diameter (Ds) is

430 defined as the diameter of the circle having the same area as the segmented ice grain. The main steps of Fig. 11 are visually

431 summarized in Fig.12 for a rimed, columnar particle.

432

433

434

Scan → background subtraction → intensity equalization → Region growing (with normalized-intensity range: 0.2-1)

Image Segmentation and Labeling (8 pixel -connected regions) ← "majority" correction (all pixels surrounded by 4 other "one" pixels are set to "one"). ← Image closure (10 pixels)

Selection of the largest labeled region → Creating the best adapted, rotated Feret bounding box → Image rotation (horizontal box) → Image resize to CNN input size 224*224

Feret's length, width, Aspect Ratio

Feret box surface-equivalent diameter

Standard measurements :

projected surface (S)

surface-equivalent diameter (Ds).

shape parameters

(Eccentricity, Euler Number, circularity, roundness, solidity, compactness, form factor, skeletal branches)

Fig. 11: The image-processing flow chart.
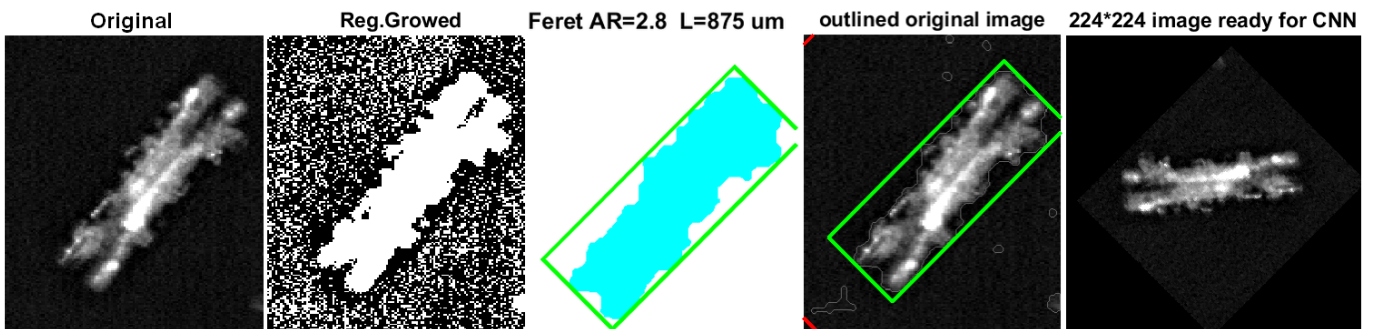
Fig. 12: The original image (in this case a rimed column) is segmented using 'region-growing'. The projected particle area (clear blue) is calculated. The bounding box is determined (green) and the Feret length and width measured. The image is finally rotated to have the mayor axis horizontal, re-scaled, and resized to the CNN input size.

452

4.1.2 Summary-image of detected particles.

The bounding boxes of all individual ice particles detected in a scan are sorted by Feret length, and reassembled in a summary-image collecting all segmented particles (Fig 13). Each particle is also associated with a numerical record containing the coordinates of its bounding rectangle on the summary-image, shape parameters, time of acquisition and local weather data. In this way, the re-analysis of the summary-image is possible instead of re-processing the original, large image. The original image is ultimately removed.

Fig. 13: Example of a summary-image for a single scan.
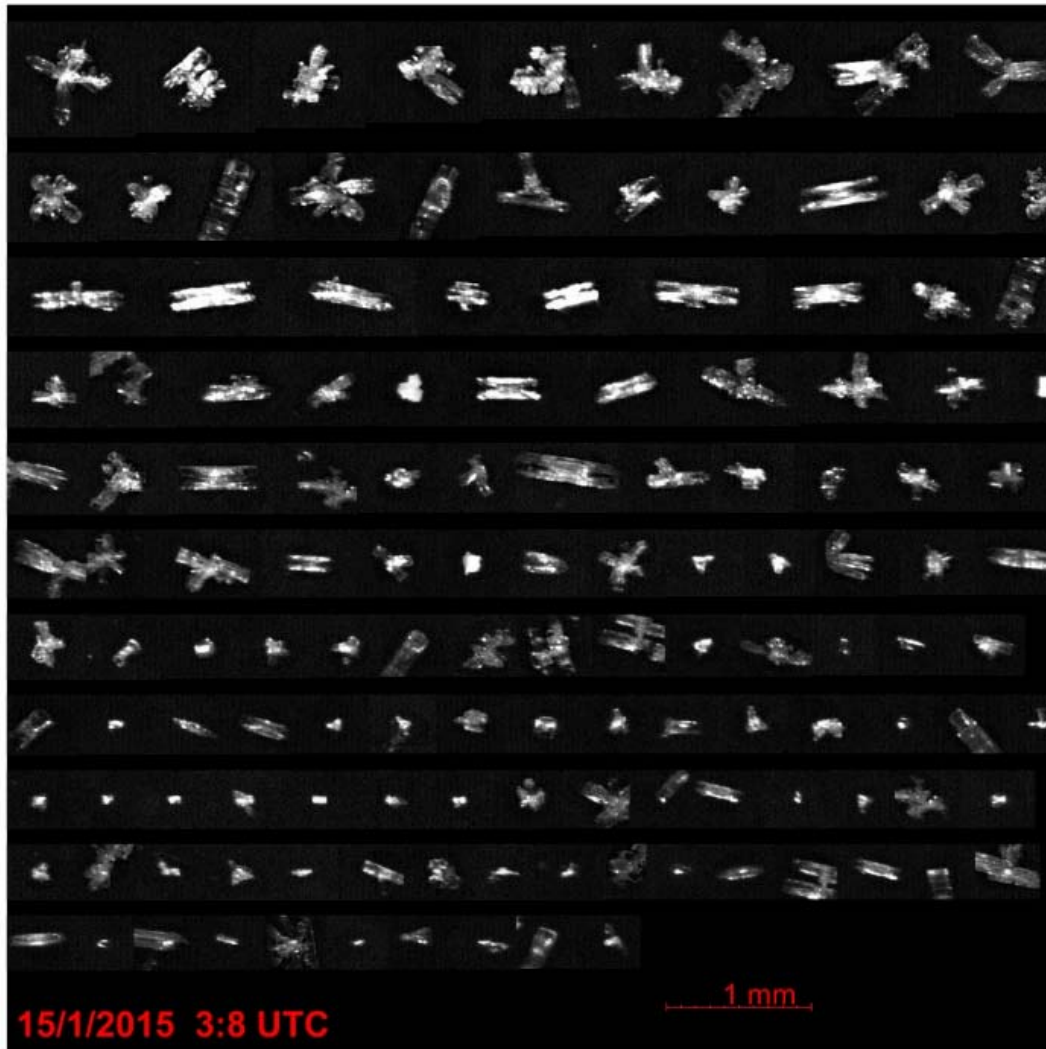
4.1.3 Limitations and uncertainties in detecting and sizing ice particles.

1) The total number of particles measured is actually limited to 2000 per scan, as a result of MATLAB memory limitations. Extra particles are not treated.

2) Particles below 3600 μm² in bounding-box surface, (equivalent to approximately 60 μm in diameter for a spherical particle) are not preprocessed (smaller particles could be detected, but most have a seemingly circular shape due to low pixelation or poor focus).

3) The segmentation becomes difficult when overlapping particles or aggregates of particles are present. In such situations, double counting of the same particle may occur in up to 12% in a scan in the presence of an intense precipitation event. The same particles can in fact fall inside different segmented areas of the image, because of the

473   lack, on the original image, of defined boundaries between particles. The process of "region growing" which leads

474   to segmented particles can actually start, independently, from several bright ("seed") regions located in different parts

475   of the image of the overlapping particles. The 'region growing' processes can then propagate through the overlapping

476   particles leading to several 'copies' of the same, segmented image. This unwanted effect could be prevented by

477   looking for similar copies of the same segmented image, but this method was not implemented at DC due to limited

478   PC resources. Overlapping particles are normally classed by the CNN algorithm as "clusters". A few occasional

479   arrangements of three or more overlapping columns are sometimes mistaken for single plates. The Feret measurement

480   of these particles is meaningless. At DC this situation occurs only after heavy cloud precipitation, a relatively rare

481   event.

482 4) Multiple counts of the same particle also occur for non overlapping particles when multiple bright spots exist within

483   the same particle. As in 3), the region-growing process can start independently from several 'hotspots', leading to

484   false copies of the same segmented particle. This effect could potentially be avoided by comparing segmented images

485   and deleting copies, but this method was not implemented at DC.

486 5) Particles close each other in the original image could be segmented into a single particle by region-growing and thus

487   misclassified.

488 6) In the case of defocused images, the particle shapes are all close to a fuzzy, round or elliptical shape, which can cause

489   a misclassification into irregular particles, spheroidal particles or plates. ICE-CAMERA images dominated by this

490   type of particles are normally eliminated during a preliminary manual screening. Also, a few big particles in summer

491   resulted rounded by partial sublimation. A few images containing only rounded or "spheroidal" particles of 500 μm

492   diameter or greater were collected during the warmest part of summer, and were manually discarded before the

493   statistical data analysis.

494 7) Needles and hexagonal plates (typically small, see Fig.23) may be very bright in ICE-CAMERA images due to

495   enhanced light diffusion at preferred angles. For the same reason, hollow columns sometimes have a shiny spot in the

496   middle. .In the case of needles, this effect can reduce the apparent aspect ratio, as the width is apparently increased

497   by the scattered light saturating the camera. For plates, the bright specular reflection blurs sometimes the polygonal

498   contour, especially in the case of small plates.

499

4.2 Automated classification of ice particles.

501 An initial attempt at automatic classification of ICE-CAMERA segmented images was made in 2014 using shape factors. This

502 kind of technique has also been used by others (e.g. Lindqvist et al., 2012) for attempting the classification of ice particles. In

503 the case of ICE-CAMERA this approach resulted extremely unreliable. A much more promising approach was offered after

504 2015 by the rapid development of transfer learning and convolutional neural networks (CNN) (Le Cun et al., 2015;

505 Schmidhuber, 2014). Xiao et al. (2019) successfully applied deep transfer learning to ice particle images obtained with airborne

506 Cloud Particle Imagers (CPI). The CNN approach has added much value to ICE-CAMERA because a reliable classification

507 of ice particles into simplified classes became possible. The CNN used for the ICE-CAMERA particle classification is

508 "GoogleNet" (Szegedy et al. 2015), a variant of the Inception network, a deep convolutional neuronal network developed by

509 Google scientists. GoogleNet is a type of convolutional neural network based on the Inception architecture. It utilises Inception

510 modules, which allow the network to choose between multiple convolutional filter sizes in each block. The GoogleNet

511 architecture consists of 22 layers (27 layers including pooling layers), and part of these layers are a total of 9 inception modules.

512 In this work, GoogleNet was used in MATLAB R2020b environment. The GoogleNet CNN, pretrained on the ImageNet

513 dataset (Deng et al. 2009), was used, with its final, fully connected layer changed to size 14. The input layer of the GoogleNet

514 architecture requires images of size 224 x 224.

515

4.2.1 The CNN classification classes.

516 Low temperatures and humidity on the high Antarctic plateau reduce the diversity of ice particle shapes. This is observed on

517 the field at DC, at South Pole station (Lawson et al., 2006), and suggested by review works such as Bailey and Hallett (2009).

519 Following an initial survey of the ICE-CAMERA image database, a set of 14 types of particles was selected, as shown in Fig.

520 14. When choosing the 14 classes, I assumed that shapes easily recognizable by a human operator could also be easily

521 recognizable by a CNN.

522

523
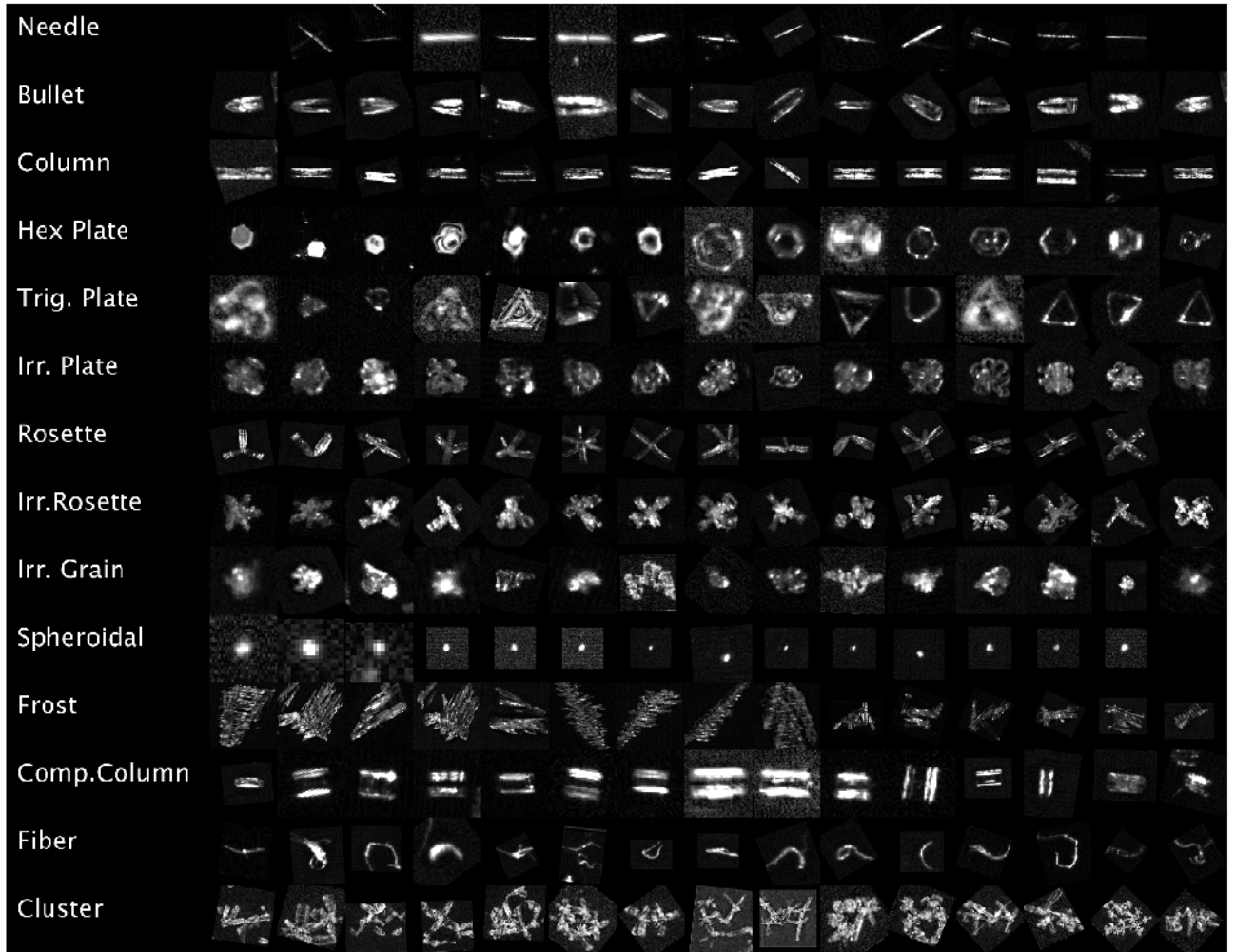
524

525 **Fig. 14: A sample of ICE-CAMERA images of the 14 classes of ice particles used to train the CNN.**

526

527 In the following scheme I tried to fit the classes chosen for ICE-CAMERA with the classification scheme of the ice particles

528 of Kikuchi et al. (2013), an updated version of the original classification of Magono and Lee (1966).

529

530 -**Needles:** covering the classes C1a,C1b,C3d   (Kikuchi et al. 2013)

531 -**Bullets:** covering the C4b-C4c classes.

532 -**Columns:** columns covering classes C2a, R2b, C3a, C3b.

533 -**Hexagonal plates:** covering classes P1a, P1b, P1c, P4f, G2a, G3a, CP3f, CP3d.

534 -**Trigonal plates:** covering the class G2b.

535   **-Irregular plates:** plate-like particles with irregularities, riming, overgrowing plates, etc. But keeping a basic hexagonal

536   shape, covering P6a, P6b, P7a, CP6d, R1b, R2b, R2c, R3a, G4b.

537   **-Rosettes:** bullet-rosettes or column-rosettes, with a minimum of two branches, covering C2c, C3e, C4d

538   **-Irregular rosettes**: rosettes with irregularities, riming, but preserving the typical stellar outline of rosettes. Covering

539   classes P7a,P7b,CP2d ,CP4c,CP5a,CP6e,CP6f,CP6g,R1d

540   **-Irregular grains:** covering CP3e, CP5a, CP6d, G4c,G4a,I3a,I2a,I1a,H1a,H1b

541   **-Spheroidal:** particles with spheroidal or spherical appearence, covering H1a, H1c. (Large particles with D>600μm)

542   detected as 'spheroidal' in DC are usually artifacts caused by defocused images and are not considered in the statistical

543   analysis.

544   **-Compact columns:** short columns covering classes G1a, C3a

545   **-Clusters of particles:** covering A1a, A3a, H2a, H1b, P8b, CP3e, CP5a, CP6h

546   -**Frost**: frost formed on the DS CP7,CP8,CP9

547   -**Fibers**: non-volatile fibrous material (from local human activities, Styrofoam particles, textile particles, dust, etc)

548

549   The last two classes are not considered in the statistical analysis of ICE-CAMERA data: they are just used to detect occasional

550   frost formed on the DS in case of super-saturation, and man-made, non-evaporable (thus persisting on the DS) materials.

551   Uncommon ice particle typologies present at Concordia were not considered in the present work. Trigonal plates have been

552   included, although they are rare, simply because they are seemingly easy to detect with CNN.

553

554   **4.2.2 The training dataset.**

555   For the training of a first CNN, a set of 5500 ICE-CAMERA segmented images of single particles, sampled randomly from

556   the 2014-2017 ICE-CAMERA database, have been manually sorted into 14 image data stores, corresponding to the 14 classes.

557   Fourteen of the computer keyboard keys were marked with the symbols of the 14 classes in order to expedite the manual

558   classification of the initial training dataset. These images were used for a first CNN training. 10% of the images were dedicated

559   to validation, 10% for testing, and the remaining 80% for training. The first CNN was used for the classification of the ICE-

560   CAMERA dataset for the years 2014 to 2017. In addition to the classification, the individual crystal images were also sorted

561   and stored in 14 folders, according to the CNN classification. Selected images from these folders were manually reclassified

562   into all 14 classes (when misclassified by CNN) and added to a second CNN training dataset. Also misclassified images were

563   thus re-labeled and used in the training dataset for the new CNN. In this way, a potential positive bias of the confusion matrices

564   due to the exclusion of misclassified images in the new training dataset was avoided. In the selection of the new training

565   images, care was taken to ensure a balanced number of training images in the 14 classes. The updated image dataset was

566   finally divided into validation (10%), test (10%) and training (80%) datasets for training a second CNN. This process was

567   repeated three times to expand the training database and thus improve the overall precision of the CNN classifier.

568   Figure 15 shows the final number of training and test images selected for each class. The total number of images used for the

569   training was 81800. Trigonal plates were rare, and their number in the training dataset was thus artificially augmented by

570   duplicating the training images, in order to avoid their absence in the small (64-images) training mini-batches.

571
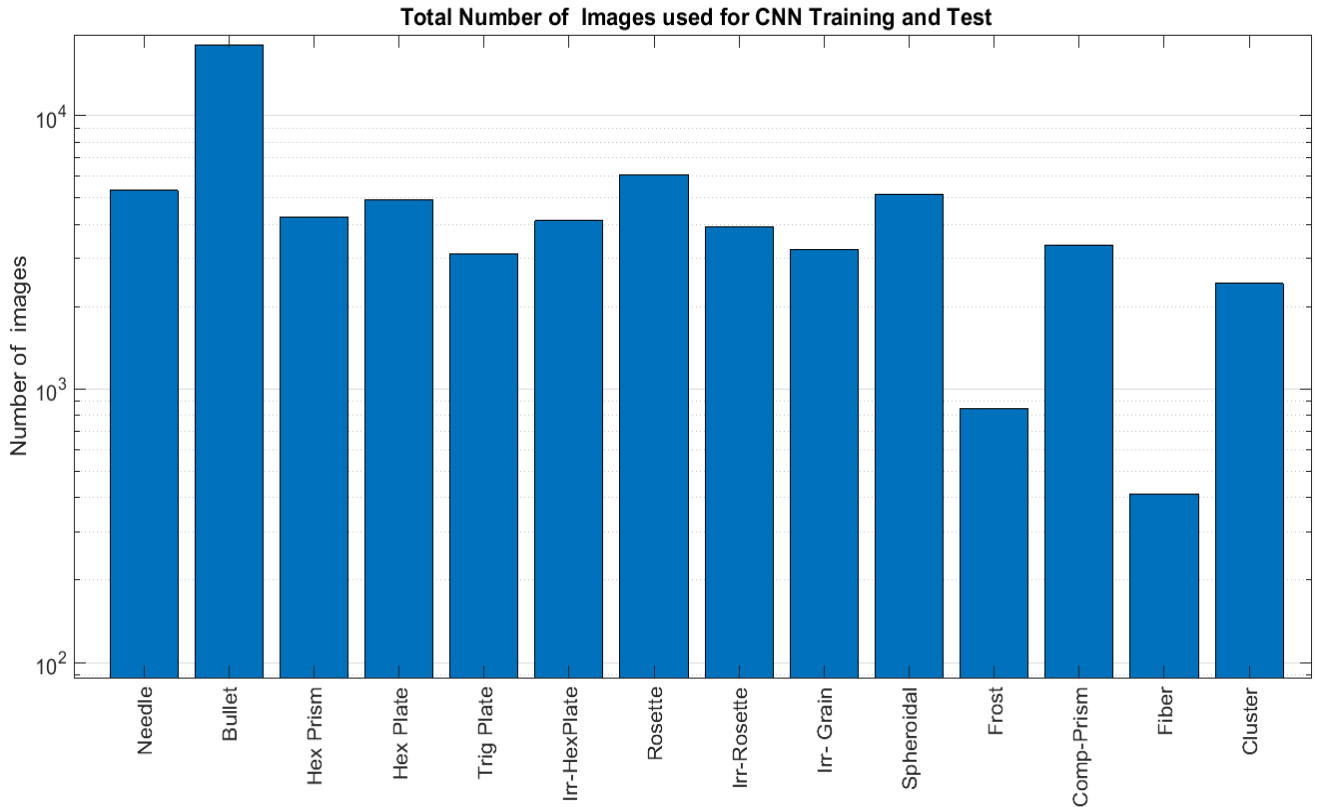
572
573   **Fig. 15: The final number of images used for CNN training + validation + test.**
574
575
576

4.2.3 CNN training details.

577

578   To meet Google's input requirements, all images of single particles were resized to 224*224 pixels. In the training process,
579   'data augmentation' was applied to the original dataset. Artificially 'augmenting' the image dataset has been shown to be
580   effective in CNN training (Shorten and Khoshgoftaar, 2019). Images inside each mini-batch are automatically, randomly
581   'augmented' in order to reduce CNN overfitting. The following transformations were used in augmentation:

582   • X, Y reflection
583   • random X, Y translations ±30 pixels
584   • Random scaling 80-120%
585   Other changes such as rotation have not been introduced since the ICE-CAMERA images to be classified are
586   typically oriented horizontally by the image processing procedure (e.g. Fig. 13)

587   The following learning options were utilized in GoogleNet training:
588
589   Solver: stochastic gradient descent with momentum (SGDM)
590   activation: softmax
591   Number of Epochs=5
592   Learn Rate=0.001
593   Batch Size=64

594   L2 weight regularization factor=0.005

595   Validation frequency= every 30 iterations

596   Shuffle of the dataset at every epoch

597   The evolution of the CNN training in terms of accuracy and losses is presented in Fig. 16. The validation line closely tracks

598   the training line, showing the absence of overfitting.
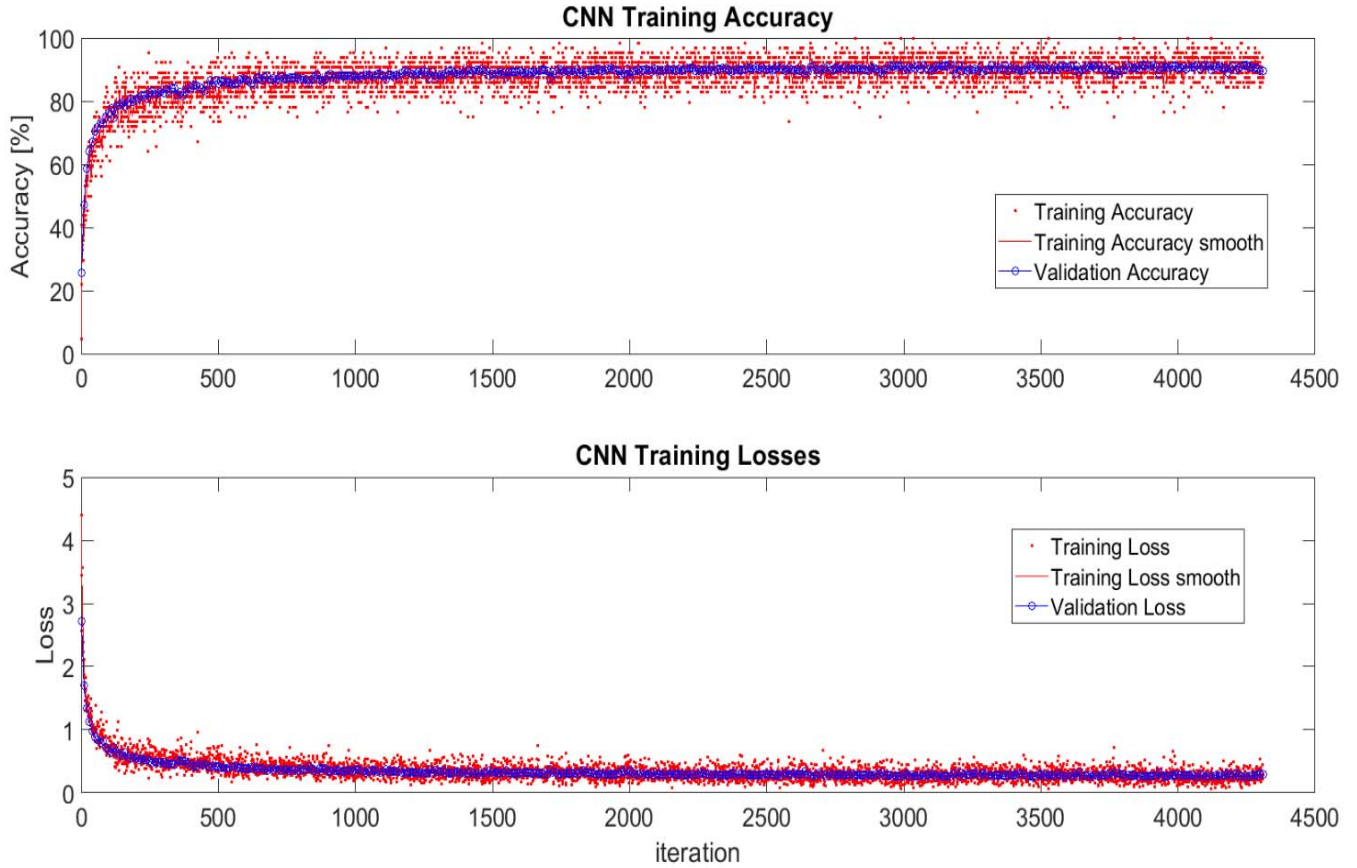
599

600   **Fig. 16: Evolution of the CNN training.**

601

602   **4.2.4. Testing the CNN classifier.**

603   CNN's performance test results are summarized in confusing matrix graphs like Fig. 17a. Each row corresponds to a

604   predicted class (Output Class) and each column corresponds to a true class (Target Class). Diagonal cells refer to correctly

605   classified observations. Off-diagonal cells are improperly classified observations (red color markings increasing

606   misclassification). The column on the far right of the plot shows the percentages of all the examples predicted to belong to

607   each class that are correctly and incorrectly classified (positive predictive value and false discovery rates, respectively). The

608   row at the bottom of the plot shows the percentages of all the examples belonging to each class that are correctly and

609   incorrectly classified (true positive rate and false negative rate, respectively).

610

611

4.2.5 Accuracy of the classifier.

In the column-normalized summary (Fig. 17a), the percentages along the i-th column shows the probability (P) of a "true" particle in class i-th being classified in each of the 14 output classes.
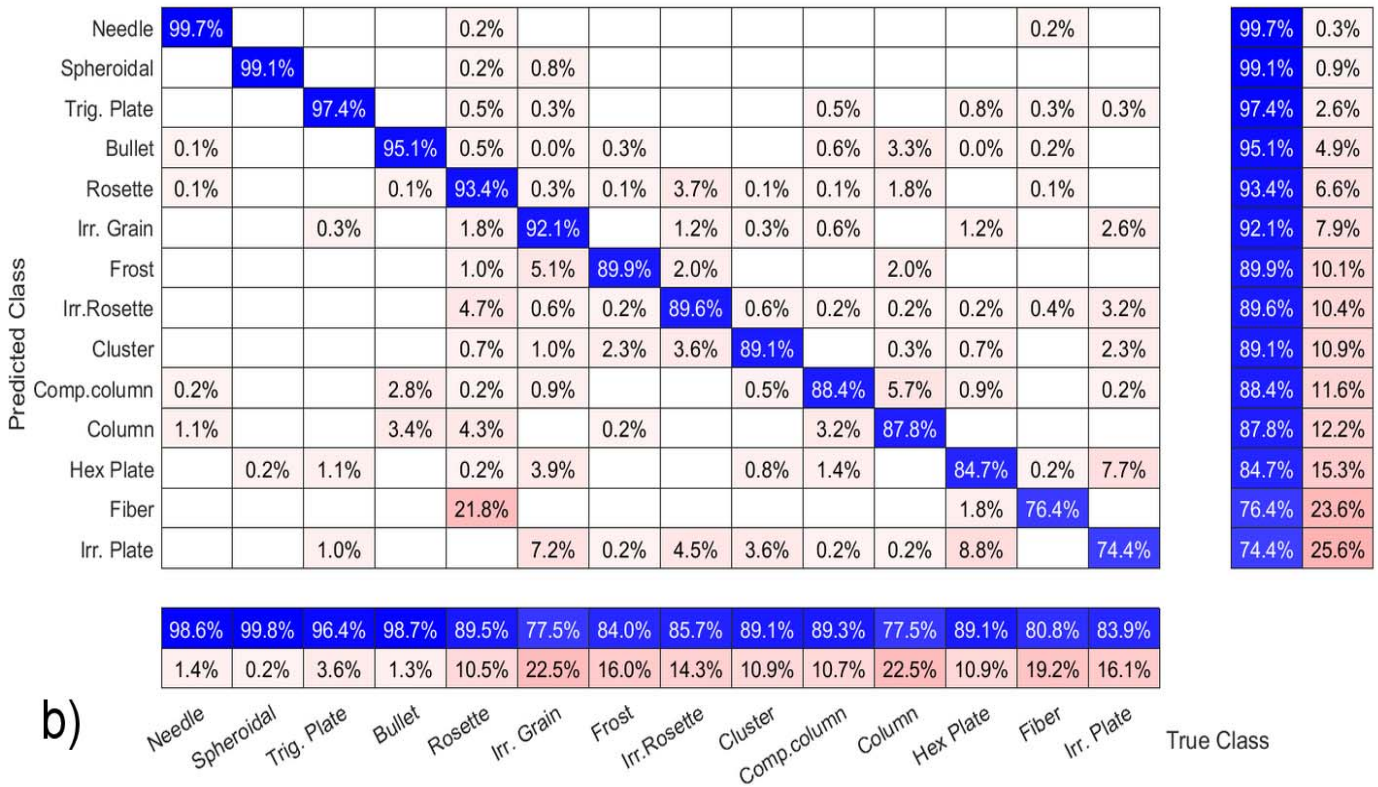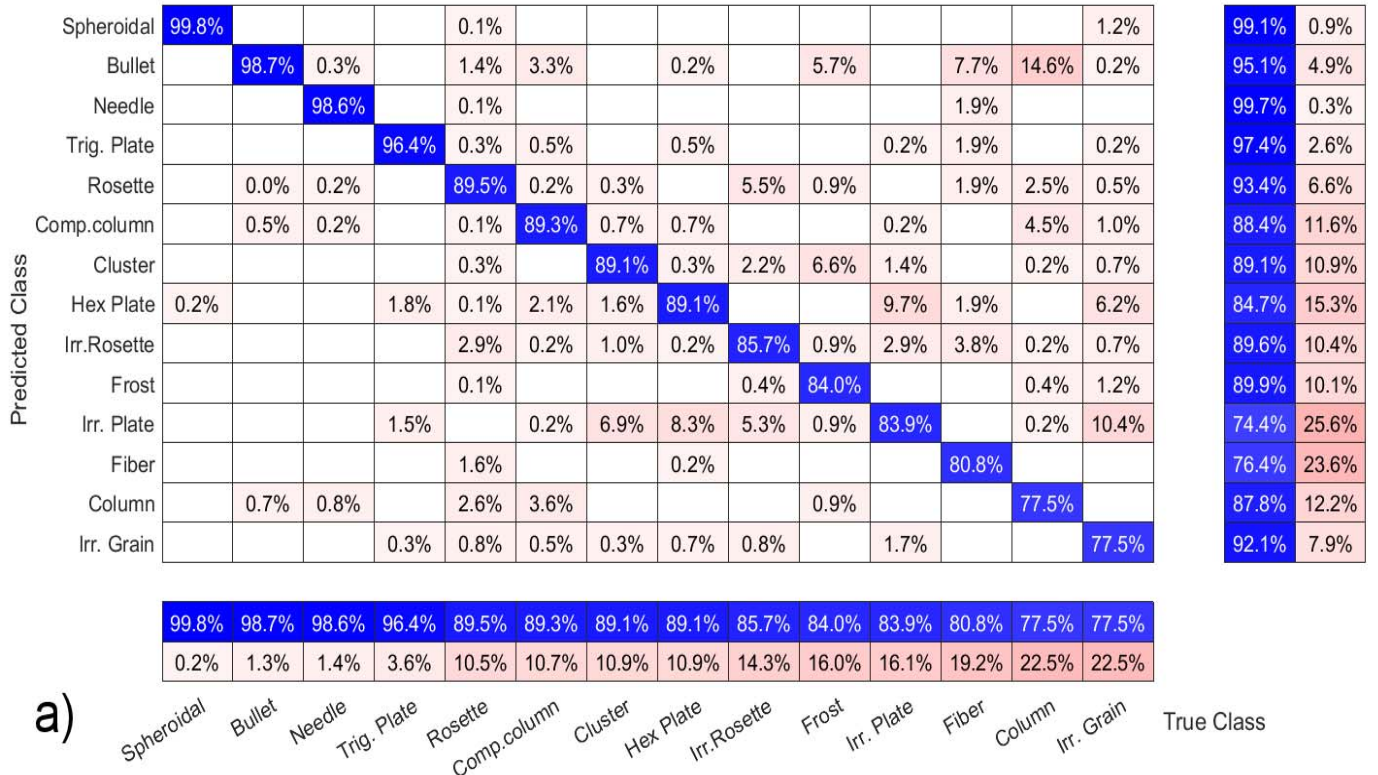
Fig. 17: Confusion plot of the CNN : a) **column-normalized,** b) **row-normalized**

617 Reading the columns of Fig 17a from left to right, the accuracy of the CNN in properly classifying a particle belonging to the

618 i-th true class (bottom row) can be assessed. The results are summarized below:

619

620 -Good accuracy (P>90%) in identifying needles, spheroidal, bullets, trigonal plates.

621 -Compact columns are misclassified into columns (3% of the time) and bullets (3% of the time).

622 -Hexagonal and irregular plates are confused approximately 10% of the time. This is expected since the edges of the plates

623 (usually small) are sometimes blurred in the image.

624 -Irregular rosettes are misclassified in 5% of cases as pristine rosettes and in 5% of cases as irregular plates.

625 -Irregular plates are confused with hexagonal plates 10% of times.

626 -Irregular grains are sometimes mistaken with irregular plates (10%) and hex plates (6%).

627 -Columns are misclassified as bullets 15% of the times.

628 The three-dimensional structure of the ice particles is lost in the ICE-CAMERA images, so that some thick ice forms such as

629 C4a, P1b, G3b, CP1a, etc. (Kikuchi et al, 2013), if any, are likely to be misclassified by this CNN.

630 A different view to read the CNN test is the row-normalized summary of the confusion matrix (Fig. 17b).

631 Percentages along the i-th row now show the probability for a particle classified into the i-th class to effectively belong to

632 each of the 14 true classes. Reading the rows of Fig. 17b from top to bottom, results are:

633 -Particles classified as needles, spheroidal, trigonal plates, bullets, pristine rosettes and irregular grains effectively (P>90%)

634 belong to their class.

635 -Particles classified as irregular rosettes have a 5% chance of being regular rosettes

636 -Particles classified as compact columns have a 6% chance of being columns.

637 -Particles classified as columns have a 4% chance of being a 2-branch rosette and 3% of being bullets or compact columns.

638 -Particles classified as pristine plates have a 4% chance of being irregular grains.

639 -Particles classified as irregular plates have a 7% chance of being irregular grains, 9% hex. plates and 5% of being irregular

640 rosettes

641 **5. Results.**

642 **5.1 Overview of ICE-CAMERA dataset.**

643 From January 2014 to December 2021, ICE-CAMERA has segmented a total of 11.007.543 particles. This gross count includes

644 particulates successively rejected for the statistical analysis. Some whole scans were eventually ignored because of poor focus,

645 sledge motor failures, or the presence of layers of snow or frost. Individual particles were omitted from the analysis due to

646 their small size or defocus. The distribution of the number of particles observed during the months is shown on Fig. 18a. The

647 number of scans per month is shown in Fig.18b. Under optimal conditions, one scan per hour is planned, with a typical total

648 of 740 scans per month. Some months, problems with ICE-CAMERA, focusing, or processing software resulted in the small

649 number of scans or particles observed. In most other cases, scans were not recorded when fewer than ten particles were detected

650 on the DS.

651

652
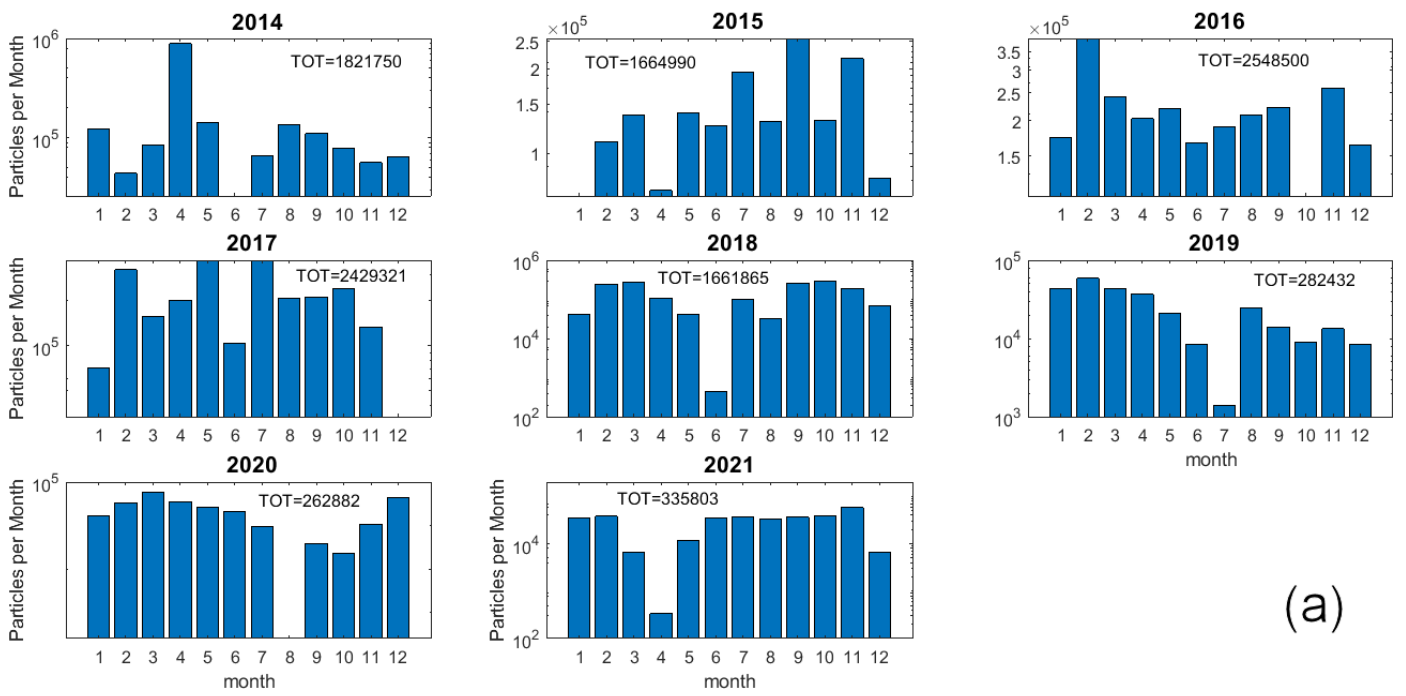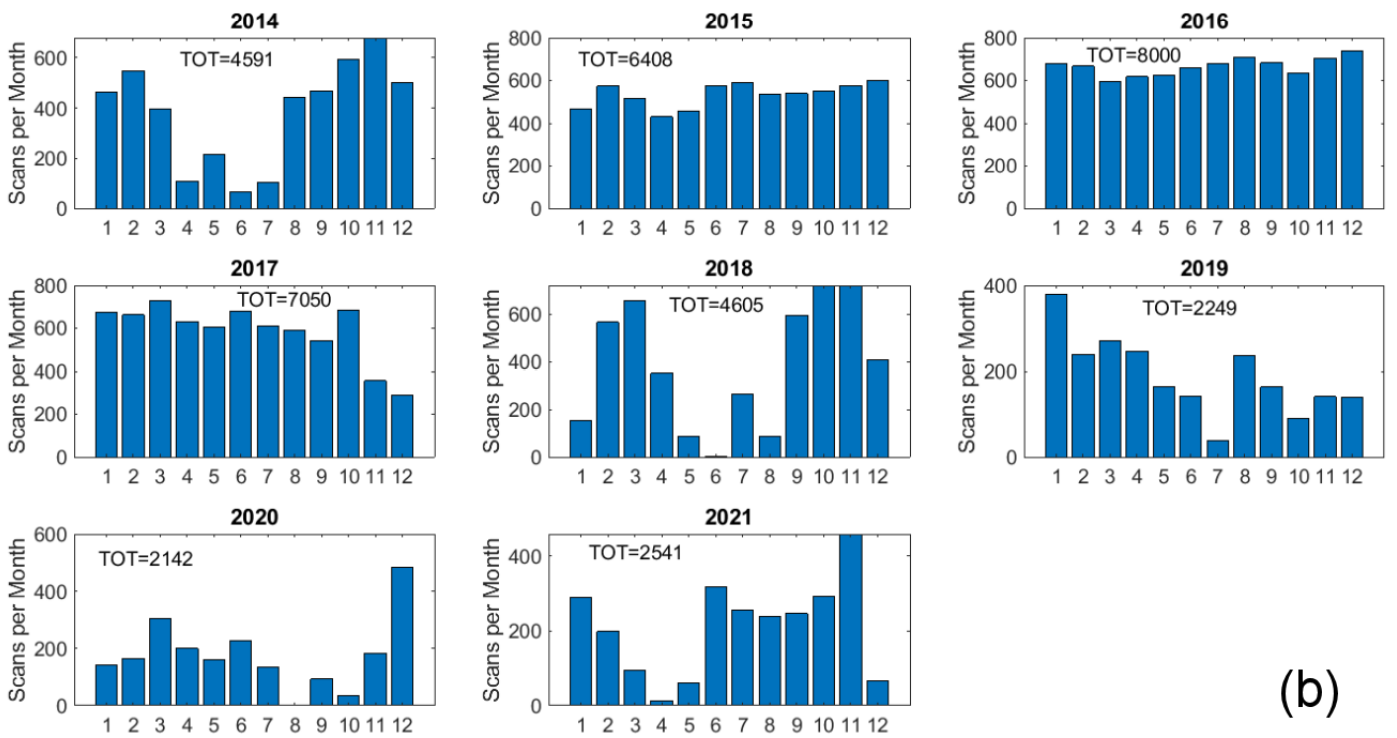
Fig. 18: Statistics per month for the years 2014 to 2021. a) Ice particle counts per month (total counts per year are also reported). (b) Number of scans per month (total number per year is also reported)

655

656   The number of particles per scan (NpS) is a rough indicator of the intensity of the collected precipitation, but it could be
657 affected by sublimation, because in condition of 'warm' air the smallest particles could disappear from the DS before being
658 detected (sec.3.2). Figure 19a shows the NpS in relation to the air temperature for the whole period 2014-2021, in box and
659 whisker format. On each box, the middle mark indicates the median, and the lower and upper edges indicate the 25th and 75th
660 percentiles, respectively. The lower and upper whiskers indicate an interquartile below the 25th percentile and an interquartile
661 above the 75th percentile.

662 Most ice particles were detected at temperatures between -60°C and -45°C, characteristic temperatures in spring and autumn.

663 The NpS at -70ºC is not statistically different from the NpS at -30ºC. This observation shows that a statistically important

664 number of particles is measured also at the highest DC temperatures, when sublimation is expected (Sect.3.2) to rapidly deplete

665 the number of collected ice particles. According with the DC air temperature statistics (fig.19d), most particles were detected

666 at temperatures above the median DC temperature.

667 Looking at NpS statistics with relative humidity (Fig. 19b), most particles were detected with relative humidity ranging from

668 40% to 50%.

669 Figure 19c shows NpS in relation to wind velocity: ice particles were collected by ICE-CAMERA under all wind conditions

670 encountered in DC. Ice particles were numerically more abundant when the wind was between 7 ms^{-1} and 15 ms^{-1}. As the

671 average surface wind speed at DC resulted around ≈6 m s^{-1} for the measurement period (Fig.19f), particles were collected on

672 the DS preferentially with winds stronger than the average, a condition typically encountered in winter in coincidence with

673 warming events (Argentini et al.,2014). These winds exceed the threshold value of 5 m s^{-1} for blowing snow at ICE-CAMERA

674 altitude, and may ultimately contain some drifting snow. The drop of NpS for wind speeds above 15 m s^{-1} (very rare in DC)

675 is probably due to the limited attachment of snow to the DS with strong winds.

676
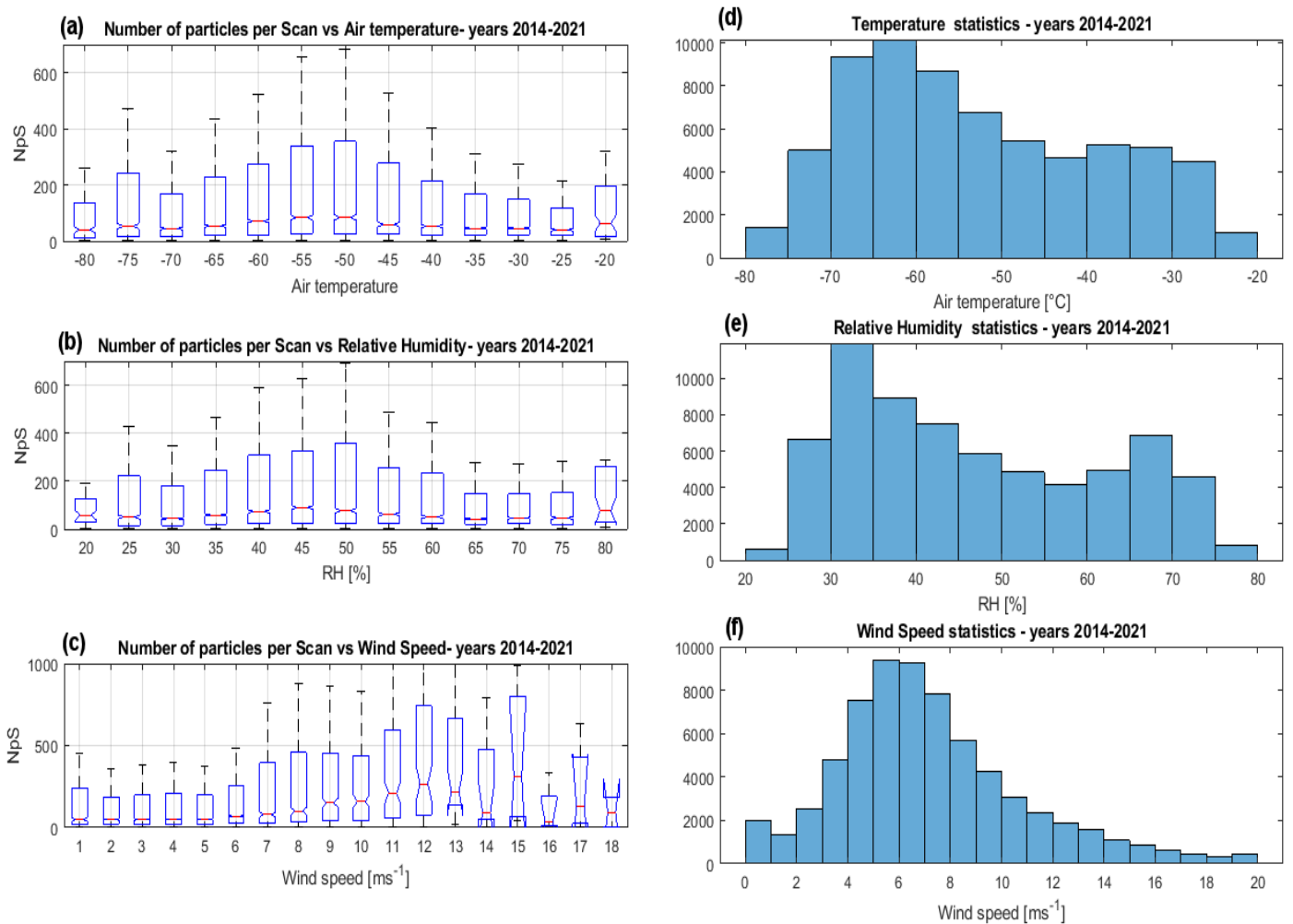
677

678 **Fig. 19: NpS statistics in relation to a)Tair, b) RH , c) wind speed.**

679 **For comparison, the statistics for d)Tair, e) RHy, and f) wind speed are shown for the same period (2014-2021).**

680

681

 5.2 Image processing and CNN used on ICE-CAMERA data.

683   MATLAB post-processing software, including the CNN classifier (Sect.4.2) and measurement tools (Sect.4.1) has been

684   applied to the 2014-2017 ICE-CAMERA dataset. Even if the detailed analysis of these data is the task of a separate paper, a

685   sample of the capacity of the instrument is presented in this section for the first two years of measurement (2014-2015). The

686   total particles analyzed resulted in N=553.358. The number of particles classified in the 14 classes is reported in Fig. 20. The

687   relative rarity of trigonal plates and spheroid particles is evident.
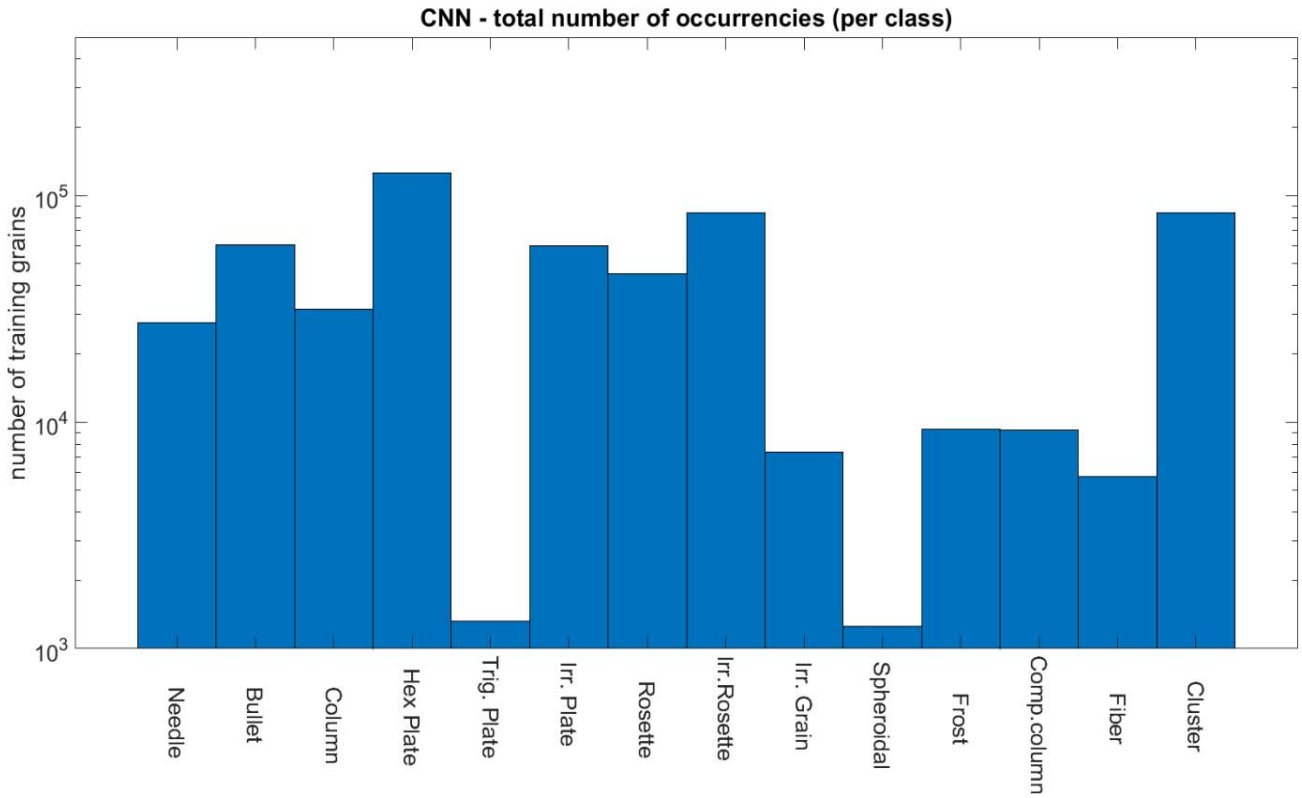
688

689   **Fig. 20: Total numbers of particles classified in the 14 classes for years 2014-2015 .**

690

691   Figure 21 shows the Feret length statistics in box and whisker format. Particles classified as plates, needles, compact columns,

692   spheroidal and irregular grains gave an average length lower than 300 μm. Bullets and columns mean length resulted in the

693   400-500 μm range, while for rosettes and irregular rosettes was in the 350-550 μm range.

694

695

696

697
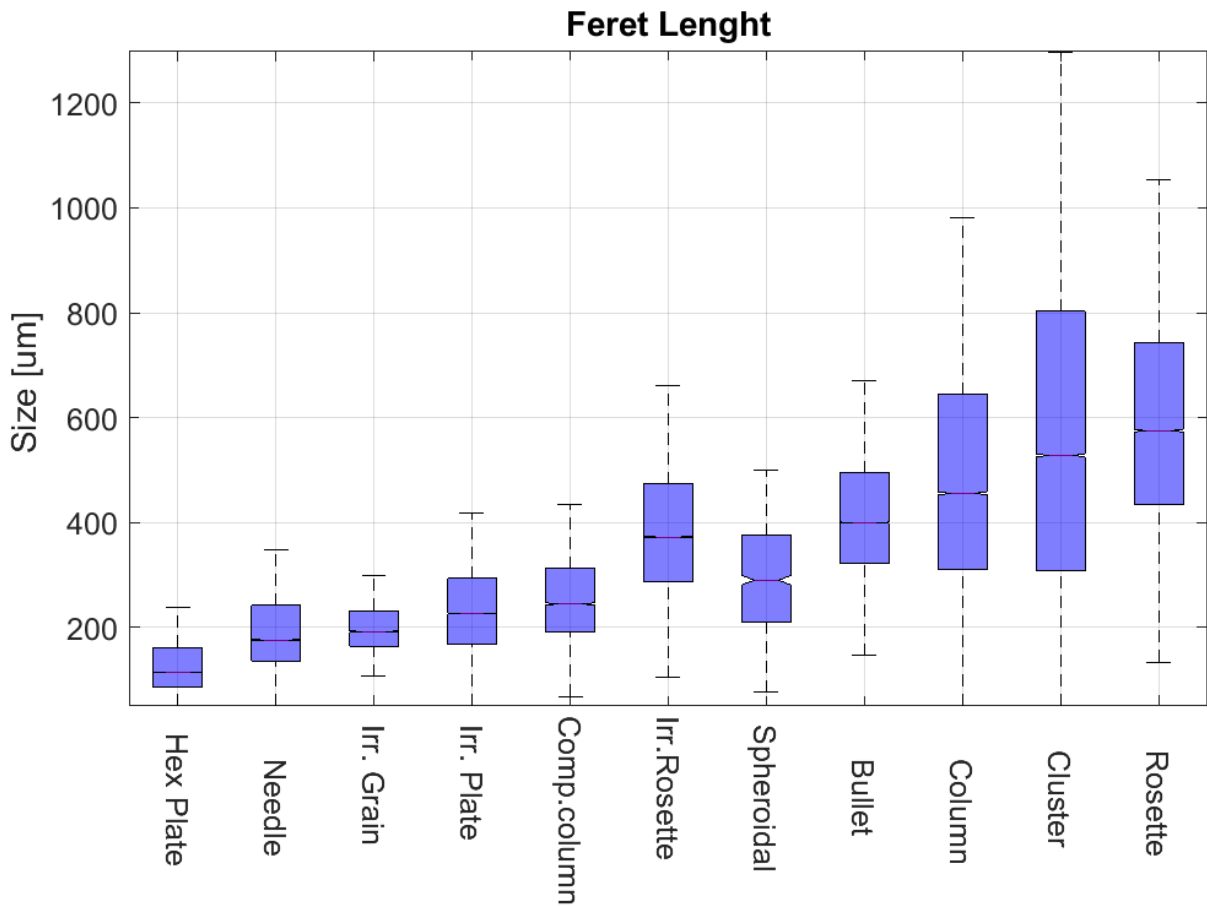
Fig. 21: Feret length statistics for the years 2014-2015

Figure 22 shows in detail the probability distribution of the Feret length for plates and rosettes. For plates (Fig22b), the peak of the distribution is for Lferet=100 μm, similar to the peak of the diamond dust (maximum) size distribution measured by Lawson et al. (2006) at SPS in summer (it must be pointed out that Lawson et al. (2006) measured also particles as small as 30 μm , while particles below 60 μm are not processed by the ICE-CAMERA software, and are therefore missing from the probability distribution of Fig22b). This finding suggests that sublimation of particles less than 100-200 μm in diameter during the deposition period (Sect. 3.2) is not relevant for shaping the final particle size statistics. The loss of particles in the lowest size range for sublimation cannot be quantitatively assessed from these data. Nevertheless, the first effects of sublimation are expected to be evident in the ICE-CAMERA images of small particles in the form of loss of sharp edges, eventually leading to spheroidal shapes (sect.3.2). An overview of the images collected in the 2014-2015 summers (where sublimation is most likely to occur) indicates that this effect is rarely observed. Either sublimation is slower than expected from the simulations of Sect.3.2, or what is observed in the summer images of ICE-CAMERA is just the result of the crystals felt just before the scan, with the majority of previously fallen small particles definitely sublimated and not detected by image segmentation. This ambiguity will be resolved in DC by taking a continuous serie of acquisitions of DD in summer conditions. The results obtained from ICE-CAMERA for pristine rosettes (Fig22a), differ considerably from those of Lawson et al (2006), because the peak of the probability distribution resulted L=480 μm, to be compared with L=120 μm of Lawson et al (2006). This difference is not explicable with the eventual sublimation of the smallest rosettes on the DS. Instead, this result is a realistic feature, sustained by the direct visual observation of rosettes in DC precipitation. A much greater amount of rosettes is actually observed in DC during precipitation from clouds than during diamond dust events. Even if rosettes in diamond dust are much
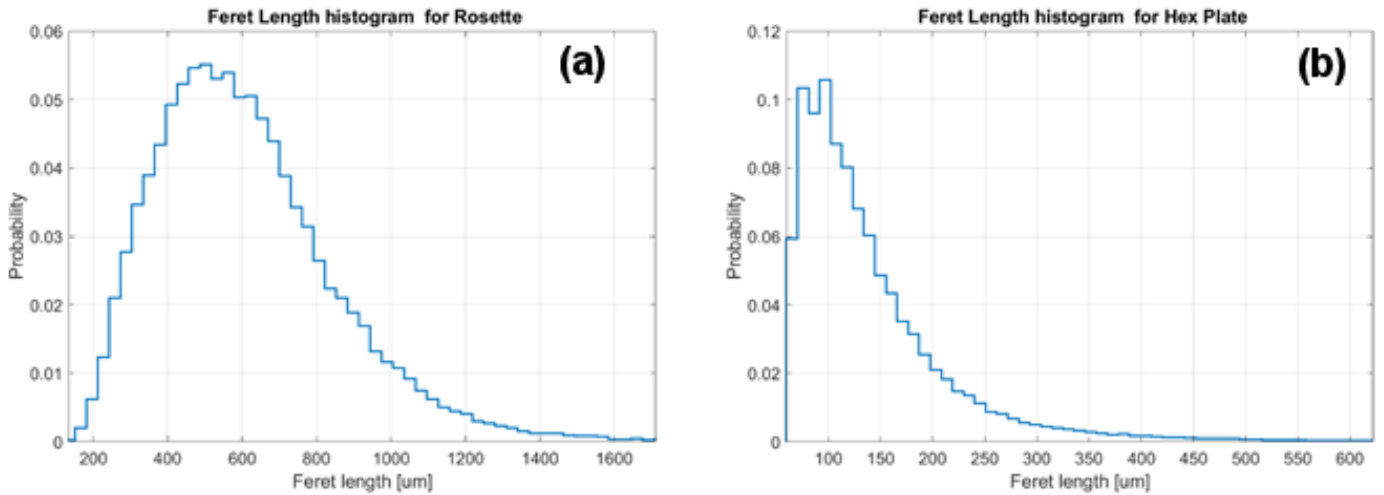
Fig. 22: Feret length probability distribution for a) rosettes and b) hex. plates. The relevant presence of small plates (D<200μm) suggests that sublimation on the DS is not relevant. years 2014-2015

Figure 23a shows Feret's aspect ratio per class. Not surprisingly, many "rounded" classes (plates, rosettes, etc.) have an AR<2. Compact columns show a median AR close to 2.4, while columns and bullets are close to 3. The average AR for the needles was 3.2, which is lower than expected for the reasons outlined in section 4.1.3.

727
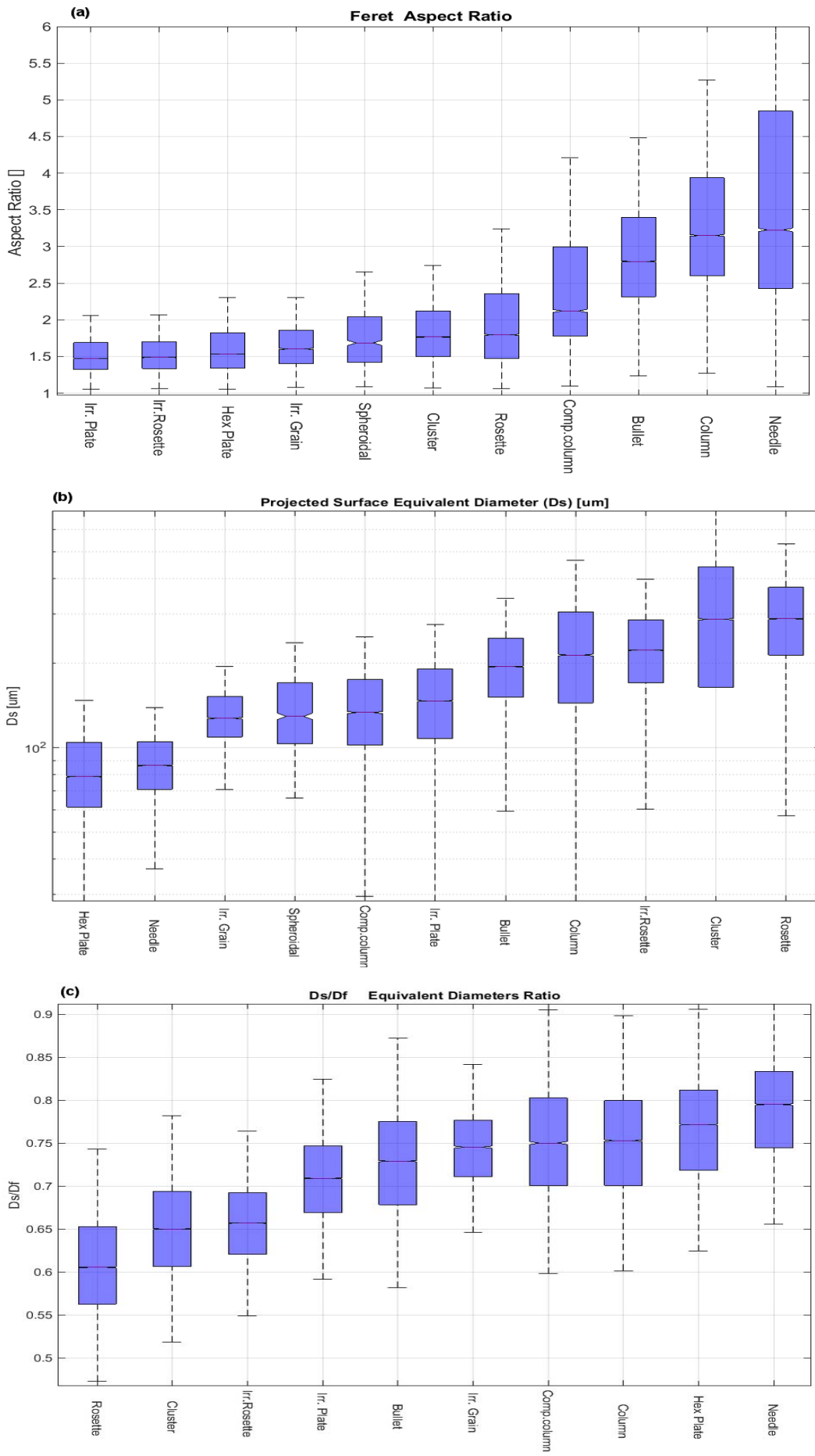
Fig. 23: Statistics of (a) Aspect Ratio, (b) Projected surface-equivalent diameter (Ds), (c) ratio between surface-equivalent (Ds) and Feret box-equivalent (Df) diameters for the years 2014-2015.

Figure 23b shows the surface-equivalent diameter Ds of the particles. Figure 23c shows the ratio between the surface equivalent diameter (Ds) and the Feret-box equivalent diameter (Df). The difference between the two diameters is relevant for "fluffy" particles like rosettes and clusters. For those particles, Ds/Df gave values of 0.6 to 0.65. For comparison, a round particle is expected to have a ratio of Ds/Df=0.89.

6. Conclusions.

ICE-CAMERA, although very similar to a simple flatbed scanner in its basic design, has represented a technical challenge for its implementation at DC. Hardware and software have been continuously and extensively modified at DC over the past five summer campaigns. The result is now a reliable instrument, running throughout the year on an hourly basis, for the statistical study of precipitation in internal polar areas. Particle size and morphology are automatically obtained, and some semi-quantitative precipitation estimates can be derived. The collected data are automatically pre-analyzed, but they can be post-processed at any time, in order to follow the continuous improvements of the image processing and machine learning algorithms. The GoogleNet CNN, trained specifically for this instrument, has succeeded in classifying ICE-CAMERA images into 14 form classes, with an accuracy of more than 80% for most of them. The instrument is particularly useful for automatically measuring the size of individual ice particles in precipitation, a process virtually impossible manually, and certainly impossible on the field in DC and elsewhere on the Antarctic plateau in winter. ICE-CAMERA scans are carried out every hour. Keeping the surface of the instrument free of frost all the time and cleaning it by heating the deposition surface after each scan is paid with the possible loss of small ice particles. Particles less than 100-200 um can disappear by sublimation before being recorded, especially in summer. This problem is complementary to the problem encountered when observing precipitation manually: when observing precipitation manually every 24 hours, (as is the case of DC) the reprocessing of particles, or the formation of ice and hoar artifacts cannot be prevented. In ICE-CAMERA, frost and ice regrowth are suppressed, but small particles may disappear for sublimation. The effect of sublimation on particles observed with ICE-CAMERA cannot be easily quantified, also given the broad range of atmospheric conditions encountered by the DS throughout the year. Images of small particles (100-200 μm) (such as plates) collected during the 2014-2015 summers rarely show evidence of early sublimation such as edge smoothing or rounding. While encouraging specific experiments with ICE-CAMERA, this observation suggests that sublimation could be slower than predicted by simulations. ICE-CAMERA data, collected since 2014, have already been statistically processed and the results will be described in a specialized paper. Results from a subset of data (years from 2014 to 2015), was presented in this work. As preliminary results, in DC the rosettes were found to be significantly larger (480 μm) than those observed at SPS by Lawson et al (2006), while the plates were of similar size (120 μm). These results demonstrated the capability of the instrument to classify and size individual ice particles in DC precipitation. Unfortunately, only non-polluted, very cold, low humidity, low precipitation environments (like high mountain tops, dry polar environments) could house a similar instrument. In the presence of pollution, marine aerosols or dust, manual cleaning of the DS would be required to remove solid particles and salts escaping sublimation. For coastal zones, the temperature is generally close to zero, making the thermal cleaning of the DS by sublimation problematic. In these environments, if an instrument like ICE-CAMERA were installed, a mechanical wiper would replace the heated glass of the current instrument. Furthermore, the CNN presented in this paper should be re-trained with different classes of ice crystals.

7. Technical issues.

Using ICE-CAMERA at DC, as well as other automated instruments, was difficult. The instrument had several failures along years, and each one was difficult to fix, at least in winter, when the instrument had to be dismounted from the roof of the shelter at -70°C and eventually fixed in the local lab by the winter-over crew, with remote assistance from Europe. Until a few years ago, communicating with DC was limited to email with small attachments, making remote assistance a lengthy task. Even today, connecting the rest of the world remotely with the ICE-CAMERA PC, to operate with the instrument software, is virtually impossible. Most hardware failures in DC were due to software bugs or computer failures. Rather than having trouble with low temperatures, operating in DC means dealing with limited heat-dissipation of PC parts such as power supply and hard disks, electrostatic discharge issues in low-humidity, heated environments, lack of spare parts for most of the year, a varied skill-ness of winter-over personnel. Failures in the thermal control of ICE-CAMERA caused some mechanical stress and failures in the focusing sledge, while water condensation eventually rusted the bearings of the stepper motors (all bearing were de-greased for a better low temperature operation). The CNN used to classify ICE-CAMERA images is continually changing and improving and the CNN training dataset increases with time, as new images collected by ICE-CAMERA are used as new training ones.

8. Code and Data availability.

The CNN developed as part of this work (under Mathworks MATLAB R2020B), along with the image dataset (224*224 images for the 14 classes of particles) used for training, validation and testing the CNN are available in the ZENODO repository (Del Guasta, 2022)

Acknowledgements.

I am grateful to the Italian Antarctic Project PNRA for supporting this work with the projects ICE-CAMERA (PNRA 2009/A4.1) and PRE-REC (PNRA 2013/AC3.05). I am also grateful to the 'Osservatorio Meteo-Climatologico Antartico' (PNRA 14_00100) for the Meteo data, and to all the logistics staff and winter-over crews of Concordia station, all working hard to permit our scientific activity. I am also grateful to Francesco Castagnoli (INO CNR) for the initial design of the instrument.

References.

Aristidi, E.: An analysis of temperatures and wind speeds above Dome C, Antarctica, Astronomy and Astrophysics, 430, 739–746, https://doi.org/10.1051/0004-6361:20041876, 2005.

Argentini, S., Pietroni, I., Mastrantonio, G., P., V. A., Dargaud, G., and Petenko, I.: Observations of near surface wind speed, temperature and radiative budget at Dome C, Antarctic Plateau during 2005, Antarct. Sci., 26(1), 104–112, https://doi.org/10.1017/S0954102013000382, 2014.

Bailey, M.P. , Hallett, J.: A Comprehensive Habit Diagram for Atmospheric Ice Crystals: Confirmation from the Laboratory, AIRS II, and Other Field Studies, J..Atm..Sci., 61, 2888–2899, https://doi.org/10.1175/2009JAS2883.1, 2009.

Bracci, A., Baldini, L., Roberto, N., Adirosi, E., Montopoli, M., Scarchilli, C., Grigioni, P., Ciardini, V., Levizzani, V.,Porcù, F.: Quantitative Precipitation Estimation over Antarctica Using Different *Ze-SR* Relationships Based on Snowfall Classification Combining Ground Observations. Remote Sens. 2022, 14, 82. https://doi.org/10.3390/rs14010082, 2022.

Böhm, H. P. : A General Equation for the Terminal Fall Speed of Solid Hydrometeors, Journal of Atm.Sci. 46, 15 , 2419-2427, accessed Oct 7, 2022, doi:10.1175/1520-0469(1989)046<2419:AGEFTT>2.0.CO;2, 1989.

Bromwich, D. H.: Snowfall in high southern latitudes, Rev. Geophys., 26(1), 149–168, https://doi.org/10.1029/RG026i001p00149, 1988.

Chokshi, A., Tielens, A. G. G. M., and Hollenbach, D.: Dust Coagulation, The Astrophysical Journal,. 407, 806,. doi:10.1086/172562. 1993.

Del Guasta, M.: CNN for the classification of ICE-CAMERA images of Antarctic ice particles, Zenodo [code], https://doi.org/10.5281/zenodo.6822140, 2022.

Deng,J. Dong,W., Socher R., Li,L-J., Li,K., and Li, F-F.: ImageNet: A large-scale hierarchical image database, IEEE Conference on Computer Vision and Pattern Recognition, 248-255, https://doi.org/10.1109/CVPR.2009.5206848, 2009.

Eidevåg,T., Abrahamsson, P.., Eng M., and Rasmuson A.,Modeling of dry snow adhesion during normal impact with surfaces, Powder Technology, 361, 1081-1092, https://doi.org/10.1016/j.powtec.2019.10.085, 2020

Fujita, K., Abe, O.: Stable isotopes in daily precipitation at Dome Fuji, East Antarctica, Geophys. Res. Lett., 33, L18503, https://doi.org/10.1029/2006GL026936, 2006.

Garrett, T. J., Fallgatter, C., Shkurko, K., Howlett, D.: Fall speed measurement and high-resolution multi-angle photography of hydrometeors in free fall, Atmos. Meas. Tech., 5, 2625–2633, https://doi.org/10.5194/amt-5-2625-2012, 2012

Genthon, C., Six, D., Gallée, H., Grigioni, P., Pellegrini, A.: Two years of atmospheric boundary layer observations on a 45-m tower at Dome C on the Antarctic plateau, J. Geophys. Res. Atmos., 118, 3218– 3232, https://doi.org/10.1002/jgrd.50128, 2016

855 Genthon, C., Veron, D. E., Vignon, E., Madeleine, J.-B., Piard, L.: Water vapor in cold and clean atmosphere: a 3-year dataset
856 in the boundary layer of Dome C, East Antarctic Plateau, Earth Syst. Sci. Data, 14, 1571–1580, https://doi.org/10.5194/essd-
857 14-1571-2022, 2022.

858

859 Grazioli, J., Tuia, D., Monhart, S., Schneebeli, M., Raupach, T., and Berne, A.: Hydrometeor classification from two-
860 dimensional video disdrometer data, Atmos. Meas. Tech., 7, 2869–2882, https://doi.org/10.5194/amt-7-2869-2014, 2014.
861

862 Grazioli, J., Genthon, C., Boudevillain, B., Duran-Alarcon, C., Del Guasta, M., Madeleine, J.-B. and Berne, A.: Measurements
863 of precipitation in Dumont d'Urville, Adélie Land, East Antarctica, The Cryosphere, 11, 1797–1811,
864 https://doi.org/10.5194/tc-11-1797-2017, 2017.

865

866 Grazioli, J., Madeleine, J.B., Gallée,H., Forbes, R.M, Genthon,C., Krinner ,G., Berne, A. Katabatic Winds Diminish
867 Precipitation Contribution to the Antarctic Ice Mass Balance. *PNAS*, https://doi.org/10.1073/pnas.1707633114, 2017.

868

869 Grazioli, J., Ghiggi, G., Billault-Roux, AC and Berne A.: MASCDB, a database of images, descriptors and microphysical
870 properties of individual snowflakes in free fall. *Sci Data* **9,** 186. https://doi.org/10.1038/s41597-022-01269-7, 2022.

871

872 Ham,F.S.:Shape-preserving solutions of the time-dependent diffusion equation, Quart..Appl.Math. **17**,137-145
873 https://doi.org/10.1090/qam/108196, 1959.

874

875 Heymsfield, A. J., Protat, A., Bouniol, D., Austin, R. T., Hogan, R. J., Delanoë, J., Okamoto, H., Sato, K., van Zadelhoff, G.,
876 Donovan, D. P., Wang, Z: Testing IWC Retrieval Methods Using Radar and Ancillary Measurements with In Situ Data, Journal
877 of Applied Meteorology and Climatology, 47(1), 135-163. Retrieved Jun 28, 2022, https://doi.org/10.1175/2007JAMC1606.1,
878 2008.

879

880 Hiley, M. J. , Kulie, M.S., Bennartz R.: Uncertainty Analysis for CloudSat Snowfall Retrievals, Journal of Applied
881 Meteorology and Climatology, 50, 2 ,399-418, 2011.

882

883 Hogan, A. W.: Summer Ice Crystal Precipitation at the South Pole. ,J. of Appl. Meteorol.,14, 2, 246-248,
884 https://doi.org/10.1175/1520-0450(1975)014<0246:SICPAT>2.0.CO;2, 1975.

885
886 Huffman, G. J., Adler, R. F., Morrissey, M. M., Bolvin, D. T., Curtis, S., Joyce, R., McGavock, B., Susskind, J.: Global
887 Precipitation at One-Degree Daily Resolution from Multisatellite Observations. Journal of Hydrometeorology 2, 1, 36-50,
888 https://doi.org/10.1175/1525, 2001.

889 Hu, MK.: Visual pattern recognition by moment invariants, Information Theory, IRE Transactions, 8, 179-187,
890 https://doi.org/10.1109/TIT.1962.1057692, 1962.

891 Jambon-Puillet, E., Shahidzadeh, N. and Bonn, D.: Singular sublimation of ice and snow crystals. Nature Commun. 9**,** 4191.
892 https://doi.org/10.1038/s41467-018-06689-x, 2018.

893 Kikuchi, K., Hogan A.W.: Properties of Diamond Dust Type Ice Crystals Observed in Summer Season at Amundsen-Scott
894 South Pole Station, Antarctica, J. of the Meteorol. Soc. of Japan. Ser. II, 57, 2, 180-
895 190, https://doi.org/10.2151/jmsj1965.57.2_180, 1979.

896 Kikuchi, K., Kameda, T., Higuchi, K., Yamashita, A.: A global classification of snow crystals, ice crystals, and solid

897 precipitation based on observations from middle latitudes to polar regions, Atmos. Res.,132,460–472,

898 https://doi.org/10.1016/j.atmos.res.2013.06.006, 2013.

899

900 Konishi H., Muramoto K., Shiina T., Endoh T., Kitano K.: Z-R relation for graupels and aggregates observed at Syowa

901 station, Antarctica. Proc. NIPR Symp. Polar Meteorol. Glaciol.,5 ,97-103,1992.

902

903 Lachlan-Cope, T., Ladkin, R., Turner, J., & Davison, P. :Observations of cloud and precipitation particles on the Avery Plateau,

904 Antarctic Peninsula. Antarctic Science, 13(3), 339-348. https://doi.org/10.1017/S0954102001000475,2001.

905 Lamb, D.,Hobbs, P. V.: Growth Rates and Habits of Ice Crystals Grown from the Vapor Phase, Journal of Atmospheric

906 Sciences, 28(8), 1506-1509, https://doi.org/10.1175/1520-0469(1971)028<1507:GRAHOI>2.0.CO;2, 1971.

907 Lawson, R. P., Baker, B. A., Zmarzly, P., O'Connor, D., Mo, Q., Gayet, J., Shcherbakov, V. Microphysical and Optical

908 Properties of Atmospheric Ice Crystals at South Pole Station, Journal of Applied Meteorology and Climatology, 45(11),

909 1505-1524. https://doi.org/10.1175/JAM2421.1, 2006.

910 LeCun, Y., Bengio, Y., Hinton, G.: Deep learning. Nature ,521, 436–444, https://doi.org/10.1038/nature14539, 2015.

911

912 Libbrecht ,K.G.: The physics of snow crystals. Rep. Prog. Phys., 68, 855–895, https://doi.org/10.1088/0034-4885/68/4/R03,

913 2005.

914

915 Libbrecht, K.G.: Physical Dynamics of Ice Crystal Growth. Annual Review of Materials Research. 47.

916 https://doi.org/10.1146/annurev-matsci-070616-124135, 2017.

917

918 Libois, Q., Picard, G., Arnaud, L., Morin, S., and Brun, E.: Modeling the impact of snow drift on the decameter-scale

919 variability of snow properties on the Antarctic Plateau, J Geophys Res Atmos, 119, 662–681,

920 https://doi.org/10.1002/2014JD022361, 2014.

921

922 Lindqvist, H., Muinonen, K., Nousiainen, T., Um, J., McFarquhar, G. M., Haapanala, P., Makkonen, R. and Hakkarainen,

923 H. : Ice-cloud particle habit classification using principal components, J. Geophys. Res., 117, D16206,

924 https://doi.org/10.1029/2012JD017573, 2012.

925

926 Liu, G.,Deriving snow cloud characteristics from cloudsat observations,J. Geophys. Res. Atmos., 113 , D00A09,

927 https://doi.org/ 10.1029/2007JD009766, 2008.

928

929 Magono, C., Lee, C. W.: Meteorological classification of natural snow crystals. J. of the Faculty of Sci., Hokkaido

930 University. Series 7, Geophysics, 2(4), 321-335, 1966.

931

932 Nelson, J.: Sublimation of Ice Crystals, Journal of the Atmospheric Sciences, 55(5), 910-919. https://doi.org/10.1175/1520-

933 0469(1998)055<0910:SOIC>2.0.CO;2, 1988.

934

935 Ohtake, T. and Yogi T.: Winter ice crystals at the South Pole. Antarct. J. U.S., 14, 201–203, 1979.

936

937 Palerme, C., Kay, J. E., Genthon, C., L'Ecuyer, T., Wood, N. B., and Claud, C.: How much snow falls on the Antarctic ice
938 sheet?, The Cryosphere, 8, 1577–1587, https://doi.org/10.5194/tc-8-1577-2014, 2014.

939

940 Palerme,C., Claud C., Dufour,A., Genthon,C., Wood N.B., L'Ecuyer,T.: Evaluation of Antarctic snowfall in global
941 meteorological reanalyses, Atmospheric Research, 190, 104-112, https://doi.org/10.1016/j.atmosres.2017.02.015,2017.

942

943 Pratt, W. K.: Digital Image Processing: PIKS Scientific Inside, Fourth Edition, John Wiley & Sons, Inc., Los Altos,
944 California, https://doi.org/10.1002/0470097434, 2006.

945

946 Praz, C., Roulet, Y.-A., and Berne, A.: Solid hydrometeor classification and riming degree estimation from pictures collected
947 with a Multi-Angle Snowflake Camera, Atmos. Meas. Tech., 10, 1335–1357, https://doi.org/10.5194/amt-10-1335-2017,
948 2017.

949

950 Ryzhkin I.A.,Petrenko V.F., Physical Mechanisms Responsible for Ice Adhesion, *J. Phys. Chem. B* 1997, 101, 32, 6267–6270,
951 https://doi.org/10.1021/jp9632145,1977.

952

953 Russ, J.C. and Brent Neal, F.: The Image Processing Handbook 7th Edition, CRC Press, pp 1053,
954 https://doi.org/10.1201/b18983, 2017.

955

956 Santachiara, G., Belosi, F., Prodi, F.: Ice crystal precipitation at Dome C site (East Antarctica), Atmos. Res. 167, 108-117,
957 https://doi.org/10.1016/j.atmosres.2015.08.006, 2016.

958

959 Satow, K.: Observations on the Shapes of Snow Crystals in the Summer Season in Mizuho Plateau, Antarctica, Memoirs of
960 National Institute of Polar Research. Special issue, 29, 103-109, 1983.

961 Schlosser, E., Dittmann, A., Stenni, B., Powers, J. G., Manning, K. W., Masson-Delmotte, V., Valt, M., Cagnati, A.,
962 Grigioni, P., Scarchilli, C.: The influence of the synoptic regime on stable water isotopes in precipitation at Dome C, East
963 Antarctica, The Cryosphere, 11, 2345–2361, https://doi.org/10.5194/tc-11-2345-2017, 2017.

964 Schmidhuber, J.: Deep Learning in Neural Networks: An Overview. Neural Networks, 61, 85-
965 117,https://doi.org/10.1016/j.neunet.2014.09.003, 2014.

966

967 Schneider, U., Finger, P., Meyer-Christoffer, A., Rustemeier, E., Ziese, M., Becker, A.: Evaluating the Hydrological Cycle
968 over Land Using the Newly-Corrected Precipitation Climatology from the Global Precipitation Climatology Centre
969 (GPCC). *Atmosphere* **2017**, *8*, 52. https://doi.org/10.3390/atmos8030052, 2017.

970

971 Shorten, C., Khoshgoftaar, T.M.: A survey on Image Data Augmentation for Deep Learning. *J Big Data* 6, 60,
972 https://doi.org/ 10.1186/s40537-019-0197-0, 2019.

973 Shimizu, H., ''Long prism'' crystals observed in the precipitation in Antarctica. J. Meteor. Soc. Japan, **41,** 305–307.
974 https://doi.org/10.2151/jmsj1923.41.5_305, 1963.

975

976 Smiley, V. N., Whitcomb, B. M., Morley, B. M., & Warburton, J. A.: Lidar Determinations of Atmospheric Ice Crystal

977 Layers at South Pole during Clear-Sky Precipitation. Journal of Applied Meteorology, 19,9, 1074–1090, 1980.

978

979 Souverijns,N., Gossart,A., Lhermitte, S., Gorodetskaya I.V., Kneifel,S., Maahn,M., Bliven,F.L., van Lipzig,.P.M.:Estimating

980 radar reflectivity - Snowfall rate relationships and their uncertainties over Antarctica by combining disdrometer and radar

981 observations, Atmospheric Research,196, 211-223, https://doi.org/10.1016/j.atmosres.2017.06.001.2017,2017.

982 Szegedy,C ., Liu,W., Jia,Y., Sermanet P., Reed S.,, Anguelov D., Erhan D., Vanhoucke V. and Rabinovich A.: "Going

983 deeper with convolutions," 2015 IEEE Conference on Computer Vision and Pattern Recognition (CVPR), 1-9,

984 https://doi.org/10.1109/CVPR.2015.7298594, 2015.

985 Tremblin, P., Minier,V., Schneider,N., Durand, G. Al. , Ashley, M. C. B. , Lawrence, J. S. , Luong-Van, D. M. , Storey,

986 J. W. V. , Durand, G. An. , Reinert, Y., Veyssiere, C., Walter, C., Ade, P. , Calisse, P. G., Challita, Z. , Fossat, E. ,

987 Sabbatini, L., Pellegrini, A., Ricaud, P., Urban, J. : Site testing for submillimetre astronomy at Dome C, Antarctica, A&A

988 535 A112, https://doi.org/10.1051/0004-6361/201117345, 2011.

989 Vignon, E., Genthon, C., Barral, H., Amory, C., Picard, G., Gallée, H., Casasanta, G., and Argentini, S.: Momentum and heat

990 flux parametrization at Dome C, Antarctica: a sensitivity study, Boundary-Layer Meteorol, 162, 341–367,

991 https://doi.org/10.1007/s10546-016-0192-3, 2016.

992 Vignon, E., Genthon, C., Barral, H.,Amory, C., Picard, G., Gallée, H., Casasanta, G., Argentini, S.: Momentum- and Heat-

993 Flux Parametrization at Dome C, Antarctica: A Sensitivity Study. Boundary-Layer Meteorology. https://doi.org/

994 10.1007/s10546-016-0192-3, 2017.

995 Walden, V. P., Warren, S. G., Tuttle, E. (2003). Atmospheric Ice Crystals over the Antarctic Plateau in Winter, Journal of

996 Applied Meteorology, 42(10), 1391-1405,https://doi.org/10.1175/1520-0450(2003)042<1391:AICOTA>2.0.CO;2, 2003.

997 Walton,W.: Feret's Statistical Diameter as a Measure of Particle Size, Nature, **162,** 329–330,

998 https://doi.org/10.1038/162329b0, 1948.

999

1000 Xiao, H., Zhang, F., He, Q., Liu, P., Yan,F., Miao, L. and Yang, Z. : Classification of ice crystal habits observed from airborne

1001 Cloud ParticleImager by deep transfer learning., Earthand Space Science, 1877–1886, https://doi.org/10.1029/2019EA000636,

1002 2019.

1003

1004 Wood, N., L'Ecuyer, T., Heymsfield, A. , Stephens, G. : Microphysical Constraints on Millimeter-Wavelength Scattering

1005 Properties of Snow Particles. Journal of Applied Meteorology and Climatology. 54. 909-931. https://doi.org/10.1175/JAMC-

1006 D-14-0137.1, 2015.

1007

1008 Zheleznyak, A.G. , Sidorov, V.G.: Flatbed scanner as an instrument for physical studies,St. Petersburg Polytechnical

1009 University Journal: Physics and Mathematics, 1, Issue 2, 134-141,https://doi.org//10.1016/j.spjpm.2015.04.001. 2015.

1010